Setup and Design of a Cryogenic Testing Station with Focus on Characterization of Superconducting Devices

by

Clifford E. Plesha

A thesis
presented to the University of Waterloo
in fulfillment of the
thesis requirement for the degree of
Masters of Science
in Physics (Quantum Information)

Waterloo, Ontario, Canada, 2019

Examining Committee Membership

The following served on the Examining Committee for this thesis. The decision of the Examining Committee is by majority vote.

Supervisor:	Jan Kycia Professor, Dept. of Physics, University of Waterloo
Internal Member:	Sergei Studenikin PRO, National Research Council Adjunct Faculty, Department of Physics, University of Waterloo
Internal-External Member:	Rob Hill Associate Professor, Department of Physics, University of Waterloo

I hereby declare that I am the sole author of this thesis. This is a true copy of the thesis, including any required final revisions, as accepted by my examiners.

I understand that my thesis may be made electronically available to the public.

Abstract

The goal of my thesis was to construct a general purpose cryostat, capable of measuring multiple devices at 100 mK. This included modifying an existing SHASTA model 106 Adiabatic Demagnetization Refrigerator (ADR) by adding a new physical support structure to allow for more weight to be added to the cryostat's testing stages, as well as custom pieces of electronics, such as a room temperature programmable current source. This allowed for computer programs to be written so we could automate the data acquisition process.

We successfully measured multiple superconducting quantum interference devices (SQUIDs), with the goal of proving that our custom electronics were able to control and record the output of the SQUID. This included measuring the biasing conditions of the SQUID with the automated current sources, as well as measuring the noise temperature of a SQUID down to 300 mK. Furthermore, we measured the thermal conductivity of our new support structure for the cryostat and were able to prove that the material used was new and novel approach for high strength, low thermal conductivity in cryogenic research. We also investigated a new technique in permanently modifying the operational frequency of a SQUID, and were able to show that this new method of laser ablating the input coil could successfully shift the frequency. While the focus of cryogenic testing was on SQUIDs the cryostat itself was designed in such a way such that many types of low temperature devices could be tested within the system.

Acknowledgements

I would like to thank my supervisor, Jan Kycia, for his support, encouragement, and mentorship during my stay at University of Waterloo. I'd also like to thank the Kycia Low Temperature Group: Taylor Fraser, Tanzee Zou, Jeff Mason, Nick Cockton and David Pomaranski for their help, insight, and making the lab a fun place to work. I want to thank the past and present members of the ADMX group in Seattle, Leslie Rosenberg, Gray Rybka, Dmitry Lyapustin, Jim Sloan, Ansel LeTourneau, and especially Andrew Wagner. You all help shape me into the researcher that I am today, and I would not be in experimental physics without your support. To all my friends Galen Sheely, Billy Balmforth, Aaron Vetter, Sora Moon, Cami Cuberson, Max Cho, Stefanie Beale, Morgan Mastrovich, and many more I want to express my deep thanks. You all have helped me, pushed me, and supported me throughout this process in your own ways.

Finally, I would like to thank family. My father, Joe, my brothers, Joe and John, my Aunt and Uncle, Rhoda and John, and my cousin, Ann, for their unending support in my career and in me. Without your support and encouragement I would not have been able to do what I am doing today. Thank you.

Table of Contents

List of Tables

List of Figures

Abbreviations

ADR Adiabatic Demagnetization Refrigerator 22, 39

CC coaxial cables 50

DUT Device Under Test 19

ENR Excess Noise Ratio 36

FAA, $Fe(NH_4)_2(SO_4)_212H_2O$ Ferric Ammonium Alum 22

GGG, $Gd_3Ga_5O_{12}$ Gadolinium Gallium Garnet 22

GRT Germanium Resistance Thermometer 30

LHe Liquid Helium 19, 68–70

MSA Microstrip SQUID Amplifier 15

PCB printed circuit board 67

SMA SubMiniature version A 67

SNR signal-to-noise ratio 34

SQUIDs Superconducting Quantum Interference Devices 5

WG Washer Grounded 16

WNG Washer not Grounded 16

Chapter 1

Motivation and Summary

Over the past several decades focus of experimental physics research has been shifting, as more effort has been placed on ultra low temperature (T$< 1\,K$) measurements. Superconducting technologies, such as the goal of building a large scale quantum computer, have been making a larger impact in the physic community. Where once the idea of a superconducting computers was in the realm of science fiction, now-a-days many governments and private companies are striving to make this a reality. However, the future of superconducting electronics does not rest solely in the hands of quantum computing as there is much research being done in superconducting electronics which can be applied to other areas of research such as space based astronomy, brain sensing, low field MRI, and more [4, 3, 9]. Further advancements in older technologies, like the pulse tube cooler have made it such that "dry" cryostats are more practical for testing of sub-Kelvin technologies. To that end, my work at the University of Waterloo consisted of testing superconducting electronics as well as helping to build the experimental setup for such testing. The goal of my project was to optimize an Adiabatic Demagnetization Refrigerator (ADR) for testing various low temperature (between 1 K and 100 mK) superconducting electronics, specifically with the aim of being able to test multiple devices in a single cool-down. Where traditional cooling methods to liquid helium temperatures (4.2 K) by a dip probe can be used to characterize a subset of materials, many devices need to be at even lower temperatures to properly function. For example, the aluminum based Superconducting Quantum

Interference Device (SQUID) does not function above 1.2 K, a kinetic inductance detector needs to be cooled below 2 K and typically operates at 250 mK, and Quantum dot devices require temperatures less than 300 mK.

To achieve this goal, several aspects of the existing cryostat had to be addressed. The existing support structure needed to be replace so that more weight could be added to the testing station. Additional electronic components were built or modified to allow for testing multiple devices, as well as automation of previously used components for efficiency and ease of use. This thesis will describe the structural support of the ADR, made to increase the load weight that the system can hold; the addition of a low temperature rf switch to increase the number of components that can be used in a testing cycle; work done to automate the cool down process including the building and testing of custom components; and a separate project that describes the modification of a microstrip SQUID amplifier to increase the device's operational frequency.

Chapter 2

Theory

2.1 Superconductivity

This thesis is focused on the applications and testing of superconducting devices, therefore it is necessary to first introduce the concept and basic principles of superconductivity before we further delve into the devices. When cooled below a material dependent critical temperature, T_c, certain materials undergo a phase change to a state of matter called superconductivity. In this state, the electrons form pairs called Cooper pairs. A Cooper pair is typically formed when the movement of the electron perturbs the lattice of the material, creating a positive charge that overcomes the Coulomb repulsion force and attracts the another electron. The number of unpaired electrons decreases as a function of temperature, $\propto \exp\{-2\Delta/k_B T\}$, where Δ is the superconducting gap. Two types of superconductors exist called type-I and type-II superconductors. The effect of superconductivity, for a type-I superconductor, are the material DC resistance drops to zero; and the material expels the total permeated magnetic flux when cooled below T_c, which is called the Meissner effect. Whereas for a type-II superconductor the material does not exhibit the Meissner effect above a certain field, H_c1.

Due to Cooper pairs replacing electrons, a superconductor has zero resistance. Unlike a normal metal, where the resistance is due to the interactions between electrons mediated by

the lattice, if the superconducting gap is bigger than the thermal excitation of the lattice, $k_B T$, than the Cooper pairs will not scatter off the lattice. Due to this, a superconductor exhibits a DC resistance of zero. This is used in many aspects of research, such as in superconducting magnets, and many electronic devices, and wiring at low temperatures. For a superconducting solenoid magnet there is no ohmic heating, which allows for large currents to flow without melting the wire or causing a large heat load on the system. Furthermore, after a current has been applied, if the two ends of the magnet are joined via a superconductor, the current will persist through the magnet as long as the material remains in the superconducting state. Superconducting solenoid magnets can reach much higher fields than solenoid magnets made from normal metals. However it should be noted that while the DC-resisitivity of the material is zero, the superconductor can still exhibit a non-zero AC-impedance due to the inductance.

The Meissner effect preserves the total net magnetic flux within a superconductor. If a superconductor is cooled below its critical temperature with an initial external field, B_i, and a flux penetrating the superconductor, Φ_i (B_i and Φ_i can be zero), then the external field is changed to B_{ext}, a circulating current will form on the surface of the superconductor such that the total net flux penetrating the material, minus a small amount of volume along the surface, will be zero. The depth that the external field will penetrate the superconductor depends on the London penetration depth, λ_L, of the material. This effect is what separates a superconductor from a perfect conductor, whereas a perfect conductor will have a DC-resistance of zero, but it will not reproduce this effect. In the cryogenic research field, this property is used to great extent to shield devices from external magnetic fields. For a type-I superconductor, this effect will hold until the magnetic field exceeds the critical field, H_c, of the material. A type-II superconductor does exhibit the Meissner effect, however the phenomenon breaks down when the magnetic field is increased beyond H_{c1}, where $H_{c1} < H_c$, and a full breakdown of superconductivity when $H > H_{c2}$, where $H_{c2} > H_c$. When $H_c1 < H < H_{c2}$, the superconductor is in a 'mixed state' or 'Schubniko phase', where the material still exhibits a DC-resistance of zero, but allows an array magnetic field, or flux tubes, to penetrate the material, where each tube has a net flux of a flux quanta, Φ_0. In this state,

2.2 Superconducting Quantum Interference Devices

Superconducting Quantum Interference Devices (SQUIDs), since their inception, are a major aspect in many fields in low temperature physics, due to their sensitivity and versatility. SQUIDs can be patterned in two distinct configurations, an rf-SQUID, and a dc-SQUID. A dc-SQUID consists of a loop of superconducting material, broken in two places by Josephson junctions. An rf-SQUID also consists of a loop of superconducting material, however it only has a single Josephson junction breaking the loop. Rf-SQUIDs are not used in this thesis, and the theory of the rf-SQUID will not be covered. For further information on the rf-SQUID please refer to chapters 1.4 and 2.3 of Ref: [7]. Henceforth a dc-SQUID shall be simply referred to as a SQUID.

Before continuing describing SQUID's characteristics, it is necessary to review Josephson junctions. A Josephson junction is a type of superconducting tunnel junction, that was first studied by Giaever in 1958 and later explained by Josephson in 1962 [22]. Josephson hypothesized that Cooper pairs could tunnel between two weakly coupled superconductors. This tunneling was unique in that, up to a certain value, a current could tunnel between the two superconductors without producing a voltage difference across the junction. The I-V curve of a Josephson junction, as shown in Figure 2.1, illustrates this property. From the figure we can see that as the current, I, increases, a voltage does not develop across the junction until I reaches the value of I_c. I_c is known as the critical current. When $I = I_c$ the voltage snaps to $\pi/4V_g$, where $V_g = 2\Delta/e$, and Δ is the superconducting gap and e is the charge of an electron. As I increases even further, the Cooper pairs are broken and the junction behaves as a normal omhic junction. Figure 2.2 illustrates the tunneling of the Cooper pair across the junction. The current that does not produce a voltage is called a supercurrent. Josephson theorized that the supercurrent tunneling was related to the phase difference, γ, between the two superconductors, $\gamma = \phi_1 - \phi_2$. The supercurrent through the junction is modeled by

$$I = I_c \sin(\gamma), \tag{2.1}$$

where I_c is the maximum allowed supercurrent through the junction. I_c is a junction dependent parameter, which depends on the barrier thickness and area.

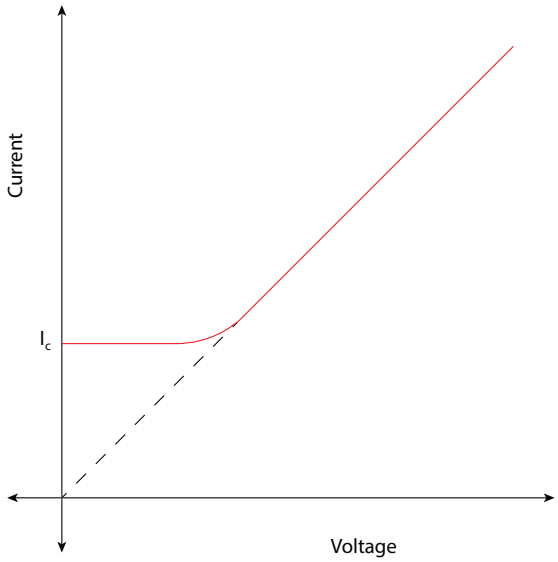

Figure 2.1: An illustration of an I-V curve of a Josephson junction.

Equation 2.1 can be rewritten as $\gamma = \sin^{-1}(I/I_c)$ for $I \leq I_c$, which illustrates that the user controlled parameter is nominally the current through the junction, and γ is the result of changing the current. Josephson further theorized that if a voltage, V, was formed across the junction then the phase difference would develop a time dependency

$$\frac{\delta\gamma}{\delta t} = \frac{2e}{\hbar}V \tag{2.2}$$

Equations 2.1 and 2.2 are known as the Josephson relations. Because the Josephson relations describe both the current and voltage in the junction, the free energy in the junction can be calculated by,

$$\int IV\,dt = (\text{const.}) - E_J \cos\gamma \tag{2.3}$$

where $E_J = \hbar I_c/2e$.

As previously state, a SQUID is a superconducting loop with two Josephson junctions, and with the Josephson relations we can examine how a SQUID operates. Similar to an isolated junction, if a current, $I_{\text{Bais}} < I_c$, is applied to a SQUID, a supercurrent can tunnel through the SQUID without developing a voltage potential.

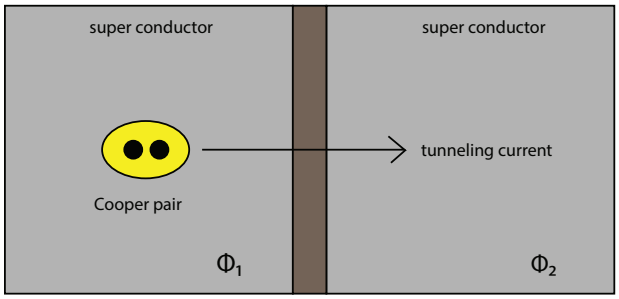

Figure 2.2: Diagram of a Josephson junction along with Cooper pair tunneling. The grey areas are superconductors and the brown area represents an insulator.

A SQUID can also exhibit hysteretic properties. As the current is increased, a voltage will develop, and the voltage will not dissipate until the applied current has been reduced to much below the critical current value. A representation of the I-V curve of a SQUID, with and without hysteresis, can be seen in Figure 2.3, where the the red line indicates the hysteretic loop. The current value at which the device switches to the zero voltage state will depend on the amount of hysteresis in the device. Depending on the SQUID, the value of I at which the device will snap back to the zero voltage state will vary, as is shown by the multiple thin red lines in Figure 2.3.

Practically, this is undesirable for a SQUID, because a well defined current to voltage characteristic is necessary. Stewart and McCumber showed that if a SQUID is patterned with an external resistor shunting both junctions and using the SQUID's internal capacitance, then the hysteresis can be eliminated entirely. To determine if a SQUID will most likely not be hysteretic, one can calculate the device's Stewart-McCumber parameter,

$$\beta_c \equiv 2\pi I_0 \frac{R^2 C}{\Phi_0} \tag{2.4}$$

where R and C are the shunt resistance and capacitance, and Φ_0 is one flux quanta which is equivalent to $\frac{h}{2e}$. In order for a SQUID to be non-hysteretic, the device should be designed such that $\beta \ll 1$, which is called the strongly overdamped limit. This corresponds to when either the value of the internal capacitance, or external shunting resistor, is small. Typically, the SQUID capacitance is only due to the junctions own self capacitance which is inherently a small value. With the additional components, the SQUID can be modeled as a

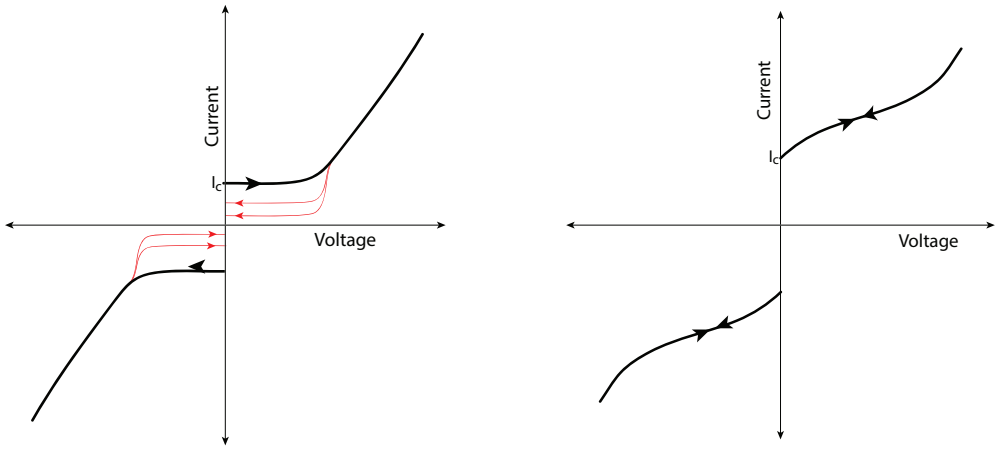

(a) (b)

Figure 2.3: An I-V Curve of a (a) hysteretic SQUID and (b) non-hysteretic SQUID.

resistively capacitively shunted junction (RCSJ) SQUID. Figure 2.5b is the equivalent circuit diagram of an RCSJ model SQUID. How the resistance in the RSCJ SQUID dampens the hysteresis can be illustrated by examining the current flow through the SQUID,

$$I = I_c \sin\gamma + \frac{V}{R} + C\frac{dV}{dt}\,, \tag{2.5}$$

which can also be written in terms of γ,

$$I = \frac{\hbar C}{2e}\ddot{\gamma} + \frac{\hbar}{2eR}\dot{\gamma} + I\sin\gamma \tag{2.6}$$

A change of variable from t to a unitless variable $\tau = t\omega_p$, where $\omega_p = (\frac{2eI_0}{\hbar C})^{1/2}$ plasma frequency of the junction can be made such that the previous equation can be written as

$$\frac{I}{I_0} = \frac{d^2\gamma}{d\tau^2} + \frac{1}{\omega_p RC}\frac{d\gamma}{d\tau} + \sin\gamma\,. \tag{2.7}$$

β can be found in the $\frac{1}{\omega_p RC}$ term. The solution to the differential equation can be written as, $U(\gamma) = -E_J\cos\gamma - \frac{\hbar I}{2e}\gamma$ and when plotted, takes the form of the well known 'tilted washboard potential' (Figure 2.4). The tilted washboard gives a good intuitive sense of the how the components in the SQUID effect the behavior of the device, as it models a

particle moving in a potential well. As I is increased, the tilt of the 'washboard' becomes more pronounced, until the particle escapes a potential well and cascades down the slope. The motion of the particle is dampened by the $1/RC$ term. If the R value is large, the dampening term will be small and once the particle moves from one potential well it will have gained even more speed when it enters the next well. This causes a runaway condition. The phase particle will not be reconfined until I is significantly reduced. It is for this reason that when fabricating a SQUID, R is designed to be small. However, this comes at a trade off, as when R is reduced the Johnson-Nyquist noise is increased. Nyquist noise, as well as other forms of noise will be further explained in section 2.7.1. This is a fabrication trade off that occurs while designing a SQUID, where the fabricator wants to make the SQUID non-hysteretic by reducing R such that $\beta \ll 1$, but also having R large enough such that there is a minimal amount of current noise in the device. Modern SQUID noise aims to be about $1\mu V/\sqrt{\text{Hz}}$ at 4.2 K. Inhomogeneities in the fabrication process can cause variance in the values of T_c, β, and the noise figure (to name a few). This is why each SQUID needs to be tested.

To understand how a SQUID operates as a flux to voltage transducer, first we must understand how a SQUID behaves in a magnetic field. Much like the Meissner effect, a loop of superconducting material has a unique function with respect to an external magnetic field, that being a superconducting ring will try to maintain a fixed value of flux within the loop. As an external magnetic field is applied to a superconducting ring, a circulating current, J, will form through the loop to counter the applied flux, ϕ_{Bias}. J will increase proportionally to ϕ_{Bias} until $\phi_{\text{Bias}} = \Phi_0/2 + \epsilon$, at which point it is energetically favorable for the SQUID to let a flux quanta to penetrate the loop and for the screening current to reverse directions. This effect is cyclical modulo Φ_0, and this effect is represented in Figure 2.6.

We can now examine how a SQUID can be used as a flux to voltage transducer. To use a SQUID in this capacity we must have the ability to bias the device with both a current, I_{Bias}, and an external magnetic flux, Φ_{Bias}. As previous explained, if then a magnetic field attempted to penetrate the SQUID, a circulating current would form. This circulating current would alter the current flowing across the junction, $I = I_{\text{Bias}} + J$, which in turn would alter γ. The voltage across the SQUID can be written in terms of the applied current

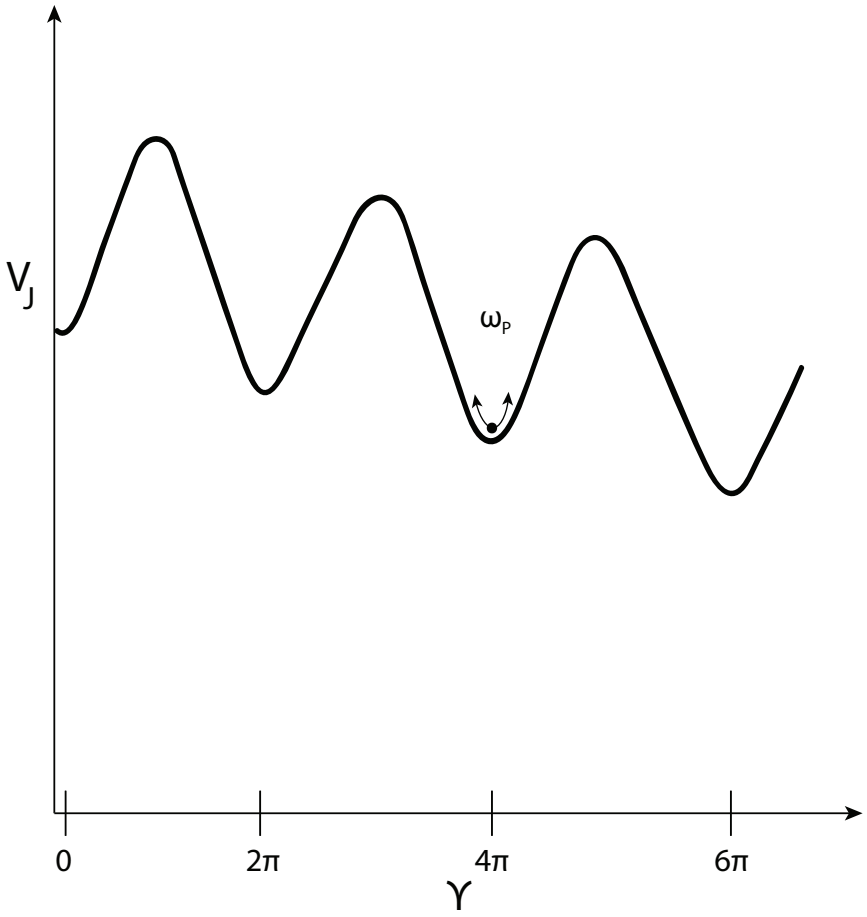

Figure 2.4: The tilted washboard potential

and the flux penetrating the SQUID

$$V = \left(\frac{R}{2}\right)\left[I^2 - 2I_c\cos\left(\pi\Phi/\Phi_0\right)^2\right]^{1/2} \tag{2.8}$$

where in this equation I is applied current through the pair of Josephson junctions ($I = I_c(\sin\gamma_1 + \sin\gamma_2)$), R is the resistance of the shunt resistors in parallel, and Φ is the total flux through the SQUID. The I_{Bias} parameters can be seen in Figure 2.7. If I_{Bias} is not large enough, then no voltage will develop across the junction, and if I_{Bias} is too large, then the small current change due to a change in the flux would be insignificant. The goal is to maximize the change in voltage with respect to change in flux. An example

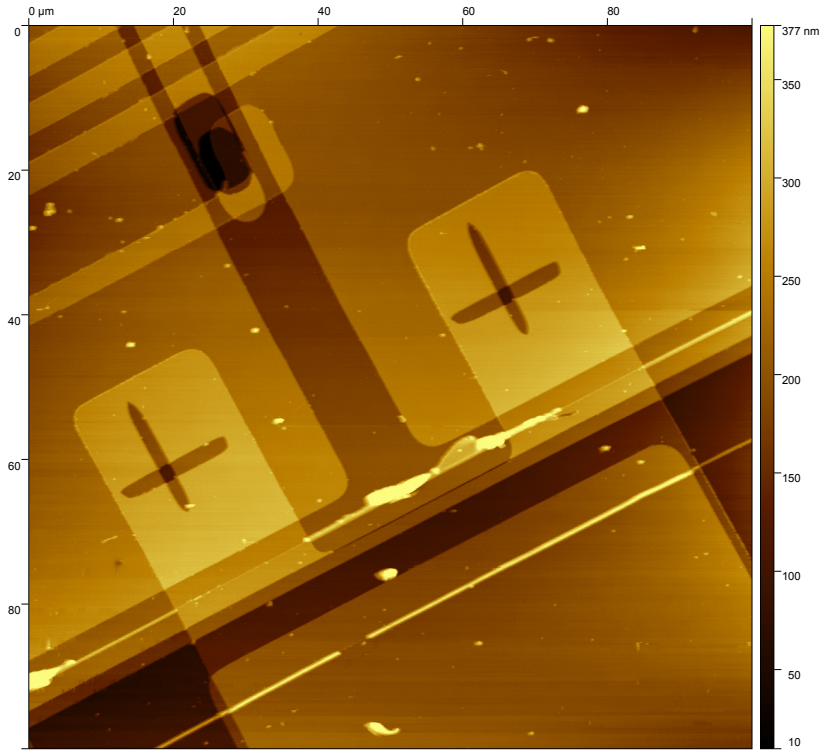

(a)

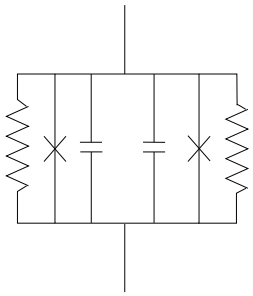

(b)

Figure 2.5: (a) An AFM image of the junctions of a SQUID. The two darker crosses are the the Josephson junctions. (b) The equivalent circuit diagram for an RCSJ model SQUID, where the X represents the Josephson junctions.

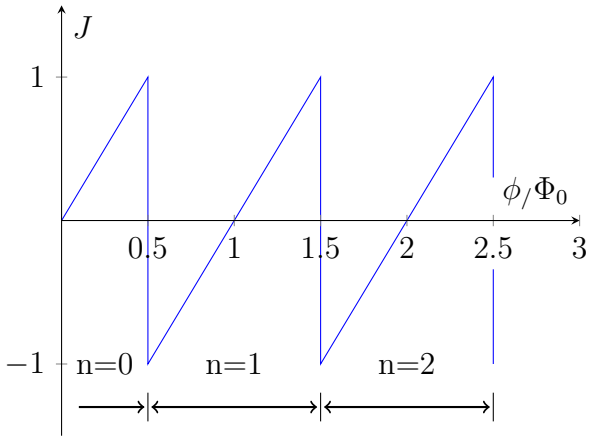

Figure 2.6: Normalized flux versus screening current, J. As the applied flux ϕ_{Bias} is applied the screening current, J, increases until a point where the current reverses direction.

graph of a SQUID's change in voltage with respect to flux can be seen in Figure 2.8. With this configuration of biasing parameters, a change in magnetic field would produce a large change in voltage. Now by understanding how a SQUID responds to a magnetic field, we can examine a common implementation of a SQUID.

SQUIDS as Amplifiers

A common use of SQUIDs is as a current amplifier. To use a SQUID as a current amplifier, an input coil is inductively coupled to the SQUID loop. The input signal is applied to the coil, which alters the value of Φ_{total} permeating the SQUID, causing a large change in voltage, which can be attributed to the strength of the input signal. In this manner, anything that produces a current can be coupled to a SQUID via the input coil. A circuit representation of a basic SQUID amplifier can be seen in Figure 2.9.

The coupling between the input coil and the SQUID is given by

$$M_i = k_i \sqrt{(LL_i)}\,, \tag{2.9}$$

where $k_i \leq 1$ is a coupling coefficient, L_i is the inductance of the input coil, and L is the

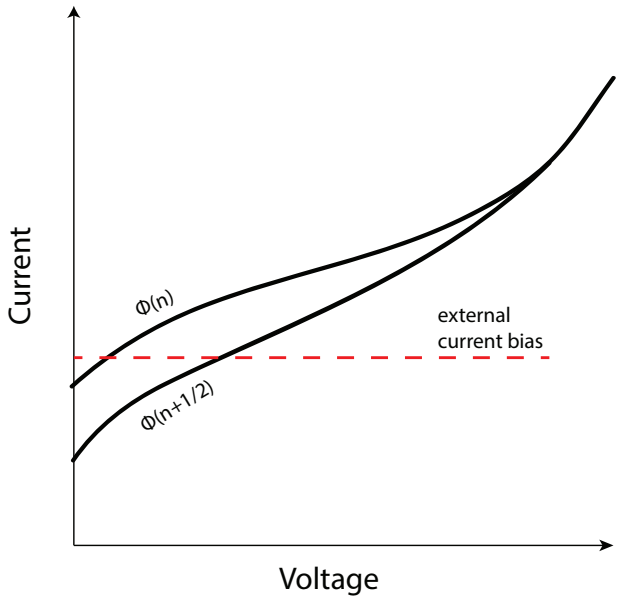

Figure 2.7: Illustration of current biasing conditions. Curves indicate the total flux penetrating the SQUID.

inductance of the SQUID. The SQUID is then biased with I_{Bias} and ϕ_{Bias} such that

$$V_\Phi \equiv \left|\frac{\delta V}{\delta \Phi}\right|_{I_{\text{Bias}}} \tag{2.10}$$

is at a maximum, as previously explained.

The gain of the SQUID can be estimated by

$$G_V = \frac{M_i V_\Phi}{Z_T^*}\,, \tag{2.11}$$

where Z_T^* is a term for the total inductance of the uncoupled SQUID minus the impedance reflected from the SQUID back into the input circuit.

Up until this point, I have illustrated a SQUID as having both junctions equidistant apart. However, SQUIDs are commonly not pattered in such a manner. For the SQUIDs used in this thesis, the two junctions are patterned closer to each other; the side of the junctions with less material is called the counter electrode side, and the larger side is

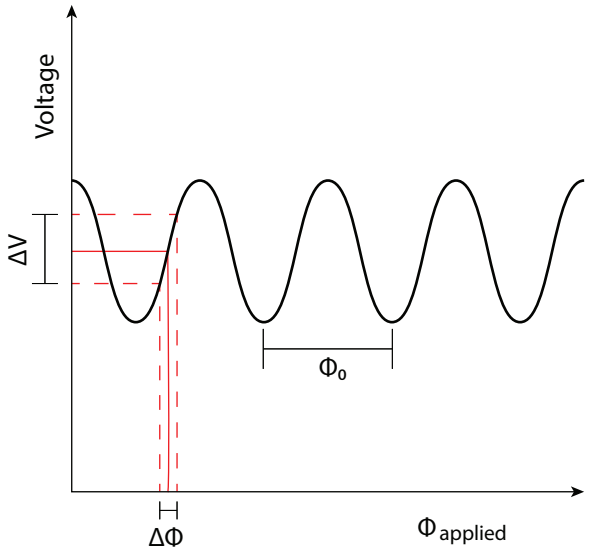

Figure 2.8: A representation of the flux to voltage characteristics of a properly current biased SQUID, where a small change in the flux, $\Delta\phi$, will induce a larger change in the measured voltage, ΔV.

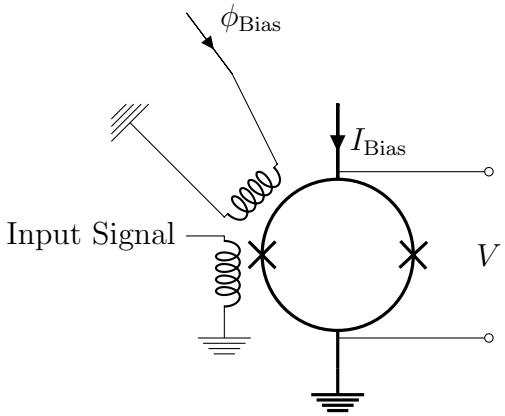

Figure 2.9: Electronic diagram of a SQUID amplifier. A current, I_{Bias}, and flux, ϕ_{Bias}, are applied; the input signal passes through a coil inductively coupled to the SQUID.

patterned as a large square with a hole in the middle and is typically called the 'square washer'. The reason for this asymmetry is to put all the position sensitive structures

near each other. This minimizes errors in aligning the multilayers during fabrication. An illustration of this SQUID pattern can be seen in Figure 2.11b.

This model of SQUID amplifier works for low input frequencies (less than 100 MHz). Above roughly 100 MHz a parasitic capacitance develops between the square plane and the input coil, causing a resonance between SQUID and input coil. This, in turn, causes a drop in the gain, and the SQUID will no longer function as a useful amplifier.

2.2.1 Microstrip SQUID Amplifiers

To increase the operational frequency range to above 100 MHz, several new SQUID patterning configurations were designed by many different research groups. The Microstrip SQUID Amplifier (MSA) is one such design, where it takes advantage of the capacitance between the input coil and the square washer (Ref [27]). (A picture and diagram of which can be seen in figure 2.11). The design principle was that the input coil, which was connected electrically to the SQUID ground in the previously mentioned configuration, is now left floating creating a microstrip. The input coil, usually referred to as the microstrip in this configuration, is patterned directly over the washer, where the coil is designed such that the width, w, is much greater that the thickness, d, $w \gg d$. The microstrip has a characteristic impedance, Z_0, defined by

$$Z_0 = \left(\frac{L_0}{C_0}\right)^{1/2} \tag{2.12}$$

where $L_0 = (\mu_0 d/w)(1 + 2\lambda/d)$ is the inductance per unit length and $C_0 = \epsilon\epsilon_0 w/d$ is the capacitance per unit length of the microstrip. When the input resistance, R_i, is greater than the characteristic impedance, $R_i \gg Z_0$, a resonance between the microstrip and square washer occurs at the fundamental frequency, which can be roughly estimated when the input signal's wavelength is equal to twice the length of the resonator [27]. However, in practice, there is no direct equation that can correctly equate the center frequency of the bandwidth to the microstrip properties, another reason why characterization of SQUID devices are necessary before implementation in an experiment.

While the coil length is a major factor in what frequency range an MSA will operate as an amplifier, the way that the device is packaged can also have an impact on its characteristics. An MSA is usually patterned on a small silicon wafer, and must be connected, or packaged, to another structure to be used in an experimental setup. The method of packing a SQUID can have an effect on the performance of the device. When packaging an MSA one can choose to either ground the square washer or the counter electrode. If the square washer is ground the MSA is in the Washer Grounded (WG) configuration, and if the counter electrode is grounded it is in the Washer not Grounded (WNG) configuration. Because of the asymmetry of the SQUID design, grounding one side verses the other has a pronounced effect on the MSA's performance. In the WG configuration, the square washer acts as a ground plane for the microstrip, however if the MSA is in the WNG configuration there is feedback from the output voltage generated on the washer and the input coil. If the voltage across the output has the same (opposite) sign as the input voltage, there is a positive (negative) feedback between the square washer and input. When the feedback is positive there is an increase in gain and the resonant frequency shifts up by about 30% [8]. For this reason, when packaging a MSA one needs to decide how to wire the device; wiring the device is explained in more detail in section 4.1.1. For more detail on SQUID design and fabrication, see chapter 3 of Ref [7].

One reason MSAs are used as first stage amplifiers, over more conventional methods, are that they have a near quantum limited noise temperature. While noise in general will be further explained in section 2.7.1, I wish to define three terms due to their importance as it pertains to MSAs. Noise is the random fluctuations in a signal,Johnson-Nyquist noise is noise generated by a current passing through a resistor, and noise temperature is measurement used to equate the amount of noise a component adds to a system to the equivent noise generated by a resistor at some temperature. In an MSA the intrinsic noise is due to the Johnson-Nyquist noise generated by the current flowing through the shunt resistors, and this current also will cause heat dissipation. As the MSA is cooled to a normal operating temperature (100 mK and below) the amount of power dissipated across this resistor decreases to around 1 nW, whereas field-effect transistor (FET) amplifiers can dissipate up to 10 mW. This difference in heat dissipation can greatly affect the operation of a cryostat at this temperature range. Also, an MSA can have the thermal noise of

50Ω resistor at 50 mK. While a high-electron-mobility transistor (HEMT) amplifier has a typical noise temperature of 2 K. The lower noise temperature allows for smaller signals to be measured. MSA have a gain of 20-30 dB and the resonance between the input coil and SQUID typically has a quality factor, Q, of roughly 10.

However, the high Q value and gain that make them ideal amplifiers causes them to have a smaller bandwidth than traditional amplifiers. While one can get a transistor amplifier that has a moderately uniform gain with a bandwidth of several hundreds of MHz to GHz, SQUID amplifiers usually do not have a bandwidth of over 50 MHz. This small bandwidth limits the use of an MSA. Research has gone into ways of altering both the bandwidth and the operational range of a SQUID amplifier, including using a varactor diode (see Figure 2.10) [28] and higher order modes of the resonance between the input coil and square washer[29].

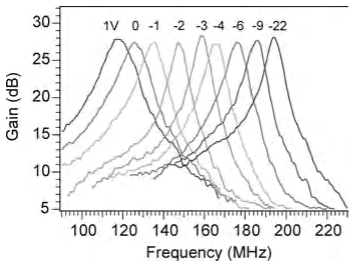

Figure 2.10: A figure from Ref: [28] showing the change in operational frequency for nine values of voltage applied to the varactor diode.

2.3 Low Temperature Refrigeration

All superconducting materials undergo a phase transition at some temperature much less than room temperature. Often superconducting materials need to be cooled below the range of temperatures reachable with liquid nitrogen (77 K) or, for some materials, below that of liquid helium (4 K). In order to reach these low temperatures, several types of refrigerators have been developed. For the main superconducting material used in this thesis, niobium, the superconducting temperature is roughly 7 K. To reach this temperature,

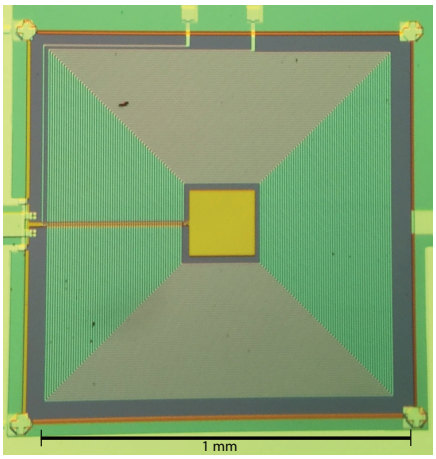

(a)

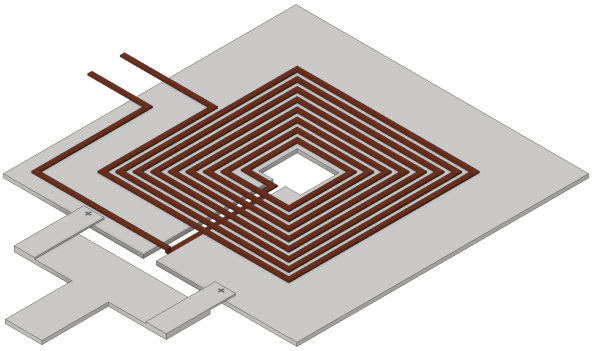

(b)

Figure 2.11: (a) A photo of a 60 turn MSA. (b) A diagram of an MSA, where the input coil is represented by the copper color, and the niobium is in grey. The Josephson junctions are represented by the crosses.

nearly all cryostats use helium in some fashion. In helium refrigeration, one can broadly define two types of refrigeration systems: wet and dry. Wet refrigerators use helium in a liquid state as a cold bath. Helium baths, pumped helium pots, and ^{3}He/^{4}He dilution refrigerators, are some examples of wet refrigeration methods. Dry refrigerators do not use liquid helium baths. Instead they use helium gas, coupled with pumping and other

techniques, to reach the temperature range of single Kelvins and below. Dry refrigerators have a practical advantage; they are a closed system, therefore the cryogens do not need to be refilled like in a wet fridge. A pulsed tube cooler is an example of a dry fridge, and is commonly used to replace a helium bath as a cold reservoir.

2.3.1 Liquid Helium

Liquid Helium (LHe) and cryogenics are inalienably tied, as for some time it has been the dominate cryogenic material used to reach the single Kelvin temperature range and below. First liquefied by Onnes in 1908, for which he won the Nobel Prize, ^{4}He, the dominant isotope of helium, boils at 4.2 K at atmospheric pressure. Because of its low boiling temperature and because it can be liquefied, LHe is commonly used in cryogenic applications as a cold bath for either dunking samples or to cool down larger components of equipment. By pumping on a bath of ^{4}He, temperatures around 1.2 K can be reached. ^{4}He is not the only helium isotope used in low temperature physics. Using the isotope ^{3}He, lower temperatures can be achieved due to ^{3}He's lower boiling point of 3.2 K at atmospheric pressure. Furthermore, by using ^{3}He in conjunction with ^{4}He in a dilution refrigerator, the milliKelvin temperature ranges can be easily reached. More on the theory and operation of a dilution refrigerator can be found in chapter 7 of Ref [34].

Helium Dewar

In order for LHe to be used as a testing environment, the liquid must be stored in a dewar, named after James Dewar, to prevent rapid evaporation. Most modern helium dewars consist of a double walled stainless steel container with a vacuum between the inner and outer walls, as well as several layers of superinsulation (thin sheets of aluminized mylar to reduce the boil off that would occur from the 300 K thermal radiation). To use helium in a research capacity, the Device Under Test (DUT) must be connected to a testing setup that can be inserted into the dewar, commonly called a dip probe. By submerging the DUT in helium we can perform tests at 4.2 K. Dip probes are used in research because it allows for testing at relatively low temperatures as well as quick turn around times between tests

compared to other cooling methods.

2.3.2 Pulse Tube Coolers

Modern pulse tube coolers play an important part in cryogenic research, as they can be used to reliably reduce the temperature of an experiment to the single Kelvin range, providing a range from $0.025 - 2$ Watts of cooling power at $4\,\mathrm{K}$ [20]. Originally proposed by Grifford & Longsworth in 1963 and experimentally achieved in 1964 [17], the pulse tube cooler is a modification of the Sterling Cycle. Whereas the Sterling Cycles uses two piston heads in conjunction to cause expansion and gas flow, a pulse tube cooler uses only a single piston to achieve a cooling effect. This modification decreases the number of moving parts, thereby reducing the chance of mechanical failure. Basic operational principle of a pulse tube cooler is that a piston pushes gas through a regenerator - a porous metal with a high heat capacity - which cools the incoming gas. The cooler gas flows into the pulse tube section, a long tube. Then during the compression cycle, the gas at the far end of the tube becomes compressed, causing that gas to become heated. This warm end is thermally connected to a cooling source such as a water pump or the ambient environment, which effectively removes the heat caused by compression. During the decompression cycle the volume expands causing a cooling effect on the gas in the pulse tube. The cooler gas then flows through the regenerator, cooling the regenerator even further. The end of the pulse tube cooler closer to the regenerator is called the 'cold head', which is thermally connected to the experimental apparatus that one wishes to cool. The pulse tube section contains enough gas such that during the compression cycle the gas has a small range of movement, therefore the gas at the cold end of the pulse tube does not interact with the warmer section of the pulse tube. This cycle is repeated until the temperature of the gas at the cold head reaches a temperature where the heat removed from the gas is equal to the heat applied from the environment. A basic diagram of a single stage pulse tube cooler can be seen in Figure 2.12. Whereas the description was for a single pulse tube cooler, it is possible to stack multiple pulse tubes together, such that the cold head of one pulse tube is thermally linked to the warm head of another pulse tube. This technique, along with further advancements in pulse tube cooler design[25] [37], is what has allowed modern

pulse tube coolers to reach below 4 K.

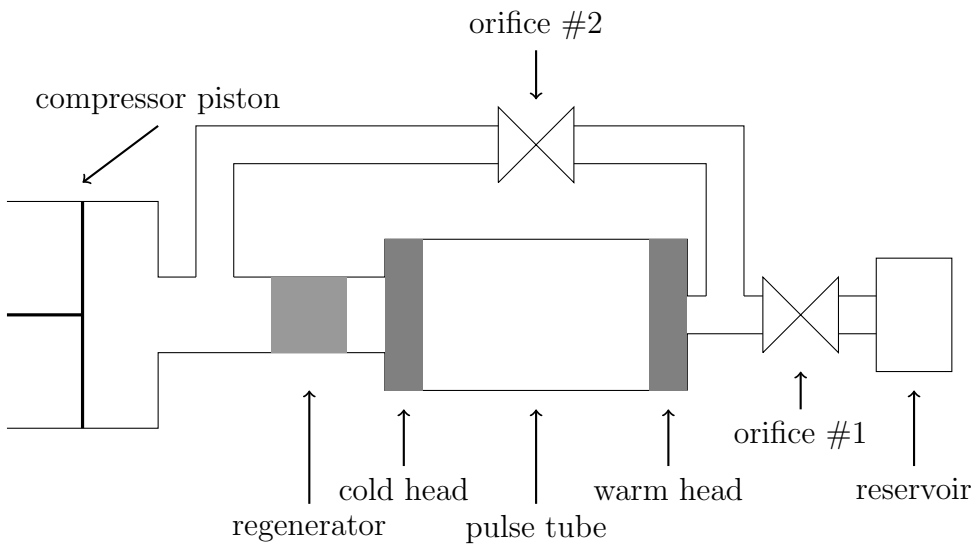

Figure 2.12: Modern design for a single-pulse tube cooler.

Due to their cooling power and low base temperature, pulse tube coolers are used in today's research to cooldown large apparatus. In our experiment we use a PT410. The capacity curve chart of this model can be seen in Figure 2.13. The cooling chart shows the two stages of this pulse tube cooler, with the first stages temperature on the x-axis and the second stage temperature on the y-axis; the wattage on the first stage determines the vertical lines, likewise the wattage on the second stage determines the horizontal line. By knowing either the temperature of the stages or the wattage on the stage, you can determine the other unknown. In our experiment we want a minimal temperature on the second stage. To do so, many components, as well as radiation shielding, are attached to the first stage. However, for our system, the main purpose of the pulse tube cooler is to reduce the temperature so we can use the secondary cooling mechanism an adiabatic demagnetization refrigerator.

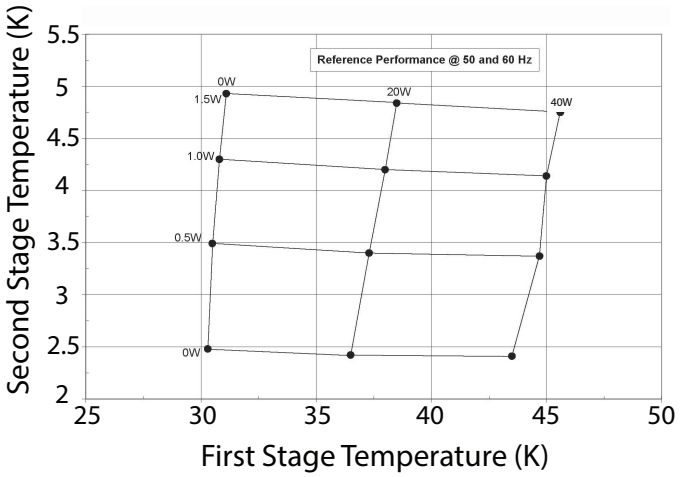

Figure 2.13: PT410 capacity curve. Figure reproduced from Ref [19].

2.3.3 Adiabatic Demagnetization Refrigerator

The second cooling method used in our experiment is an Adiabatic Demagnetization Refrigerator (ADR). An ADR is a cooling device that allows small samples to be cooled down from the base temperature of the pulse tube cooler, 2.7 K, to 50 mK without the use of any cryogenic liquid. The ADR was originally proposed independently both by Debye [12] in 1926 and Giauque[15], and then experimentally verified by Giauque & McDougle in 1933 [16] and DeHaas [11]. Instead of cryogenic liquids, an ADR uses paramagnetic salt crystals (hereby called salt pills) along with an external magnetic field to cool down a sample to sub-Kelvin temperature range, by relying on the reduction of the spin entropy of the salt pills.

An ADR consists of one or more salt pills surrounded by a solenoid magnet. The model of ADR that is used in this thesis, an HPD SHASTA 106, consists of two salt pills, a Gadolinium Gallium Garnet (GGG, $Gd_3Ga_5O_{12}$), and Ferric Ammonium Alum (FAA, $Fe(NH_4)_2(SO_4)_2 12H_2O$) salt pill. The salt pills are thermally connected to platforms called the cold rod(s), which are colloquially known as cold finger(s). The salt pills / cold fingers system are thermally connected to the rest of the system by a heat switch. A heat switch is a mechanism by which two components can be thermally connected or isolated. In this

ADR system, the heat switch is a mechanical clamp that is controlled by a stepper motor. A diagram of an ADR is presented in Figure 2.14, where we see two salt pills (a FAA pill and a GGG pill) surrounded by a magnet. The pulse tube cooler is used to reduce the temperature of the magnet and salt pills to a temperature range where we can take advantage of the paramagnetic cooling effects.

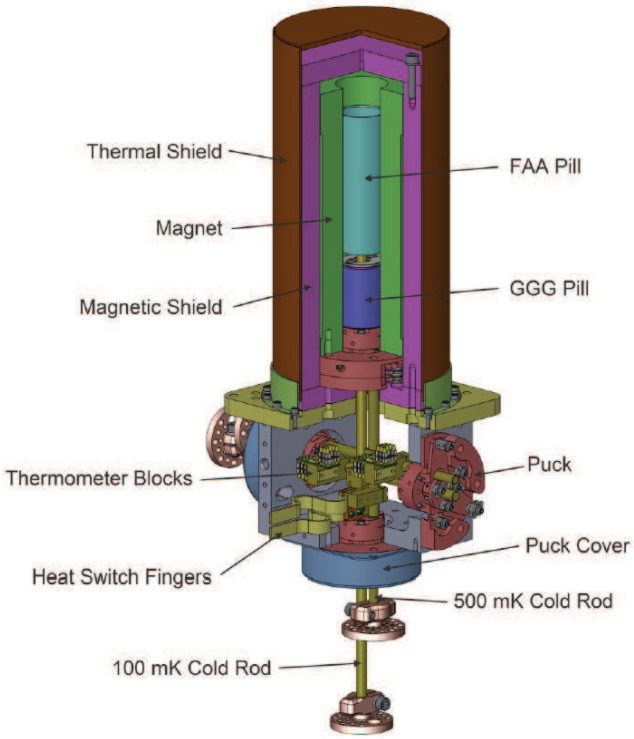

Figure 2.14: Cutaway model of a HPD SHASTA Model 106 ADR. Image reproduced from Ref [21]

When the system has been sufficiently cooled by the cold bath, the ions in the salt have some angular momentum, J, which can have a random $2J + 1$ possible orientations. The entropy of the system, S, is then given by

$$S = R \ln (2J + 1) , \tag{2.13}$$

where $R = Nk_B$ and N is the number of molecules of the salt, and k_B is the Boltzmann constant. The interaction between the spins in the salt pills is assumed to have energy much less than the thermal energy of the system, k_BT. By applying an external magnetic field, B, the moments of the salt pills will become partially aligned.

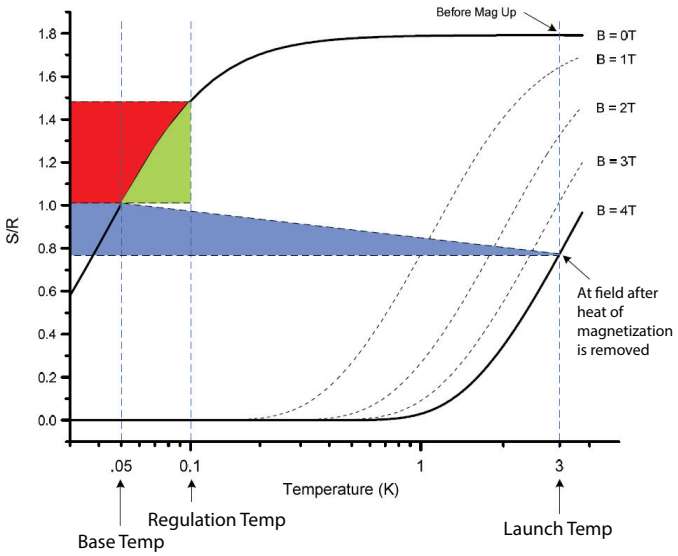

Figure 2.15: An entropy versus temperature chart of the paramagnetic salt crystals. The multiple black and dashed lines indicate the entropy curve of the salt in different magnetic fields. As can be seen, at higher applied fields the salt crystals order, reducing the entropy of the system. When the magnetic field is reduced, the temperature decreases, as indicated horizontal dashed line. The blue area represents the amount of energy it takes for the salt pills to cool down the system due to the mass connected to the cold fingers of the ADR. If the ramp is stopped at a specific field, the green area represents the energy - or entropy space - available to keep the system cool. The red area represent the amount of energy it takes to warm up the system to 100 mK. This figure is reproduced from Ref [21].

While the external magnetic field is increasing heat will be generated. This is called the heat of magnetization, which can be calculated by

$$Q(T_i) = nT_i[S(0, T_i) - S(B_f, T_i)]\,, \tag{2.14}$$

where T_i, and B_i is the field of the magnetic field before staring the cooling process, and B_f is the final magnetic field before the cooling process. When the heat is switch closed, this heat is absorbed by the cold reservoir, which in the case of our system is the pulse tube cooler. As the magnetic moments in the salt pills become more aligned, the total entropy of the salt pills decreases. After the salt pills are aligned and all heat of magnetization is removed from the system, the salt pills and cold finger system are thermally decoupled from the cold reservoir by the heat switch. At this point in time the cryostat effectively has two systems, the pulse tube cooler and magnet system and the salt pills and cold fingers system. The magnetic field is adiabatically decreased from B_i to some final field value, B'_f. As the magnetic moment becomes more disordered the entropy of the salt pill and cold finger system increases, and by the third law of thermodynamics, $\delta S = \frac{\delta U}{T}$, the temperature of the system must decrease in response. It is by this principle that the temperature of the cold fingers can be reduce to the sub-Kelvin range without the use of cryogenic liquids.

A graphical representation of the cooling process can be seen in Figure 2.15. The thick black lines indicates a salt pill's entropy to temperature relation. As the external field is applied and the magnetic moments become more aligned, the entropy of the system decreases while the temperature remains constant. Then, after the salt pills are thermally decoupled from the cold bath, the external magnetic field is reduced the total entropy of the system stays the same; therefore the temperature of the salt pills decreases. The blue area in the graph represents the increase of temperature that is caused by cooling down the excess material connected to the salt pill. As more mass is added to the system, the larger this area becomes, and by extension the system cannot reach as low of a temperature, or cannot stay at a lower temperature for as long. The green area represents the total energy available, if the demagnetization is stopped before the external field is reduced to zero. In this graph, the demagnetization is stopped when the pills reach 100 mK. The red area represents the energy it takes to warm the base system from the lowest temperature to 100 mK. The lowest achievable temperature, if there is no heat load on the system, can be approximated by

$$T_{\text{base}} \approx \frac{B_{\text{low field}} T_{\text{launch temp}}}{B_{\text{high field}}} \,. \tag{2.15}$$

However, it can be seen that if we let $B_{\text{low}} \to 0$ then $T_{\text{base}} \to 0$. In practice, this equation is only a rough approximation as the magnetic moments of the salt pills will self order at a

material dependent temperature. For the FAA this temperature is roughly 30 mK [34], and for GGG it is around 150 mK [35]; the ADR can not be cooled below these temperatures with the salt due to the self ordering.

After the magnetic field is decreased to 0 T, or there is no entropy space left, the system will begin to warm up from any applied heat. Applied heat can come from several sources which include but are not limited to; heat leaks from the cold reservoir, which is at a warmer temperature than the cold fingers and attached components; thermal radiation; any measurements which can cause heat. For this reason when constructing an ADR system several components should be taken into consideration including using salt pills with a higher J to remove more entropy out of the system. Furthermore, during the construction of an ADR system it is important to reduce the heat on the cold fingers as much as possible, thus allowing you to stay at lower temperatures for a longer period of time. Reduction of heat can be achieved by thermal sinking any wiring to the experiment to several intermediate temperature stages, and using superconducting wiring which does not transfer heat very well.

The SHASTA 106 has a large vacuum area for the experimental setup. The large area allows for a significant amount of electronics and supporting components to be attached to the cold fingers. However, the cold finger does not have a large tolerance on the amount of torque that can be applied, therefore it is unwise to attach a large mass directly to the system. If an excess amount of torque is applied, the Kevlar wire supporting the cold fingers could break causing a thermal touch between the cold fingers and the rest of the system. To utilize the available space, a support structure (much like scaffolding) can be constructed, allowing for more weight to be connected to the cold finger without fear of damaging the system. Where this support structure is physically connected to the sturdy cold plate of the pulse tube cooler. The support system does provide another heat path to the cold finger, and therefore it must be built and designed with materials that have low thermal conductivity.

2.4 Thermal Conductivity

Thermal conductivity, κ, is a material dependent property, which describes the heat flow due to a temperature gradient. It can be expressed as part of the heat flow equation,

$$\frac{dQ}{dt} = \kappa \frac{A\Delta T}{l} \tag{2.16}$$

where $\frac{dQ}{dt}$ is the rate of heat flow, A is the cross sectional area of the material, l is the length of the material, and ΔT is the temperature difference between the two measured points. The thermal conductivity is the material dependent portion of the equation. Between large temperature ranges, or in specific materials, κ can have some temperature dependence, $\kappa(T)$. Materials that are ideal for low temperature thermal isolation purposes have a small κ, such that heat flow is minimized.

Heat transfer has two main components the movement of electrons, and phonons (lattice vibrations). If the transfer of heat movement of these phonons and electrons through the material, however these heat carriers usually scatter off other electrons, phonons, or imperfections in the material. The thermal conductivity coefficient can be expressed as

$$\kappa = \frac{1}{3}\frac{C}{V_{\mathrm{m}}} v\lambda \,, \tag{2.17}$$

where v is the average velocity of the heat carrier (phonon or electron), λ is the mean free path of the heat carrying entity, and C is the specific heat of the material, where the factor of $\frac{1}{3}$ is because the equation only depicts the heat flow in a single dimension, and V_m is the molar volume of the material.

Thermal Conductivity at Low Temperatures

In the work presented in this thesis, the most relevant occurrence of thermal conductivity is the transfer of heat between different stages of the ADR. By minimizing the thermal conductance of materials attached to the cold stage of the ADR, one can reduce the base temperature and maximize the hold time per cooling cycle.

At lower temperatures, the number of thermally excited phonons is small, therefore the scattering of electrons is the dominant factor in the thermal conductivity, which scales with

T. Materials with two ends at different temperatures can have a relatively large thermal gradient, a large difference in $\kappa(T)$. Therefore, to calculate the heat flow, we must account for the change in the thermal conductivity coefficient,

$$\dot{Q} = \frac{A}{L} \int_{T_1}^{T_2} \kappa(T) dT \,. \tag{2.18}$$

When constructing a low temperature cryostat, it is vital to consider the thermal conductivity of the components. To cool down the sample, one usually wants a strong thermal link between the cold source and the sample; therefore, one has to be aware of how the thermal conductivity of the connecting material changes over a large temperature range. However, at times, a weak thermal link is also important. Physical connections between different temperature stages in a cryostat is one example. If connected with materials that have a high thermal conductivity, the thermal link could cause a large enough heat flow that the lower temperature stage may not reach the desired temperature. For this reason, the thermal conductivity of many different materials has been studied between 300 K and cryogenic temperatures.

Thermal Conductivity of Superconducting Materials

For superconducting materials, the main component of the thermal conductivity is often the unpaired electrons. While Cooper pairs are perfect electrical conductors, they all rest in the ground state, where they have zero entropy. They cannot leave this ground state to transfer any entropy and therefore they cannot carry heat. The number of unpaired electrons decreases as $e^{-2\Delta/k_B T}$. At low enough temperatures, the number of unpaired electrons becomes small enough that the phonon term once again dominates. Therefore, in this range, the thermal conductivity of superconducting material is much lower than that of normal metals. For this reason superconducting metals can be used as thermal insulators, as well as electrical wiring without causing large heat leaks.

2.5 Specific Heat

Specific heat, $C(T)$, denotes how much energy it takes to change the temperature of a given amount of material. Depending on the material, the specific heat equation will have different terms. In the following section I will focus on the specific heat of metals, due to their importance in this thesis.

Specific Heat of Normal Metals

The energy in metals can be excited by two means; either by vibration in the atomic structure, phonons, or by the free electrons in the material. The electron term of the specific heat scales as a function of the temperature, $C_{\mathrm{e}} = \gamma T$, where γ is the Sommerfeld constant. The phonon term scales as the temperature cubed, $C_{\mathrm{ph}} = \beta T^3$, and is the dominate factor of the specific heat of metals at high temperatures. Therefore one can write the full specific heat as

$$C(T) = C_{\mathrm{e}} + C_{\mathrm{ph}} = \gamma T + \beta T^3 \tag{2.19}$$

Specific Heat of Superconducting Metals

For superconducting materials, the equation determining the specific heat of the material changes from its normal state. The phonon term is unchanged as the material can still be excited via oscillations of the atoms. However, the electron term is greatly altered. First when the material enters the superconducting state there is a large jump in the electron term in the specific heat. This spike is attributed to the extra degree of freedom the electrons experience from the electrons entering the superconducting state. However, because this is a second order phase transition, there is no latent heat during this transition. This jump in specific heat can described as $\Delta C = \alpha \gamma T_c$, where γ is the term from the normal-state electron specific heat, and α is an material dependent term. After the electrons have entered the superconducting state, they can no longer be thermally excited without exiting the superconducting state, thereby decreasing the specif heat. To account for the unpaired

electrons, an exponential factor is added to the electron specific heat term

$$C_{\mathrm{e,s}} = \alpha\gamma T_c \exp\{-2\Delta/k_B T\} \tag{2.20}$$

where Δ is the energy gap in density of states. The specific heat of a superconductor can be expressed by,

$$C = C_{\mathrm{e,s}} + C_{\mathrm{ph}} = \alpha\gamma T_c \exp\{-2\Delta/k_B T\} + \beta T^3 \tag{2.21}$$

2.6 Low Temperature Thermometry

Determining the temperature of the cryostat and experimental samples is instrumental to low temperature physics. Thermometers can either be a primary or secondary type of thermometer. Primary thermometers are thermometers that use fundamental aspects of physics to determine the temperature. For example, Cobalt thermometers use the radioactive decay to determine the temperatures, and vapor pressure thermometers use the vapor pressure of liquids to determine the temperature. Secondary thermometers do not have a theoretically predictable temperature dependency. Instead there is a reproducible relationship between some measurable variable and temperature, which is used to determine the temperature. The Germanium Resistance Thermometer (GRT)s and RuO_2 thermometer are the secondary thermometers that are used in this thesis. The advantages of using such thermometers are that they are easy to implement and readout.

Doped Germanium Thermometer (GRT)

A GRT is a germanium semi-conductor that has been either doped with As or Ga to create an excess electrons or holes respectively. The germanium chip itself is supported on gold leads and encapsulated in a protective shell, with helium to act as an exchange gas between the germanium and the shell. GRT are commonly used because of their reliability after repeated cool downs. Care does need to be taken when using a GRT, as germanium has an orientation dependent magneto-resistance [34], also applying an excess of current, or a DC current, to the device can alter the doping which can permanently change the temperature

dependence. A GRT has a resistance to temperature relationship that can be described by [34]

$$\ln R = \sum_{n=0}^{m} \alpha_n (\ln T)^n \,, \tag{2.22}$$

where α are experimentally determined coefficients, and m are integers typically less than 9. The device used in the work presented was calibrated from 50 mK to 5 K by the provider, Lake Shore. While such thermometers can be calibrated down to the sub 10 mK range, their resistance starts to approach mega-ohms at which point one needs to be concerned about impedance mismatches between the GRT and the readout device, which can impact the devices reported temperature.

RuO_2 Thermometer

RuO_2 thermometers, like GRTs, are secondary temperature sensors, therefore they have several of the same advantages and disadvantages as mentioned in section about the GRT. They consist of a thin film of RuO_2 and Bi_2RuO_2 embedded in silicate glass and deposited on a substrate.

RuO_2 thermometers are easy to produce and are cheaper than GRTs, they also have a smaller, to nonexistent below 1 T, magneto-resistance making them ideal for work in a low magnetic field [34]. Furthermore, because the temperature-to-resistance function is dependent on the metal-to-glass ratio of the chip, rather than any internal doping, they are more robust than a GRT, to the point where one can measure the resistance with a standard multimeter without fear of damaging the device. Unlike the GRT, one can easily get many un-packaged devices, which can be attached to either dedicated holders or directly onto components via GE varnish. However, they are considered to be less stable than a GRT.

Like a GRT, RuO_2 thermometers can be calibrated to be used in the tens of milliKelvin to a few Kelvin range. To calibrate a RuO_2, one can fit the measured resistance to a calibrated temperature by the following equation [34]

$$\ln R = \sum_{n=0}^{2} A_n \, (\ln T)^n \tag{2.23}$$

where A_n is the experimentally determined coefficient.

2.7 Amplifier Characterisitcs

Amplifiers are a necessary component in most sensitive experimental works today. Because the purpose of the work presented here was to build a cryostat for testing various low temperature devices, amplification of small signals can play a critical role. However, like all microwave components, not all amplifiers are created equal. Different amplifiers can work in different frequency ranges, can intake different amounts of power, output various levels of noise, and so forth. To that end there are some key qualities of amplifiers that should be addressed.

The frequency range at which an amplifier is designed to function is call the bandwidth of an amplifier. The bandwidth is usually listed as the the frequency range from which the output falls off by 3 dB from the maximum gain. A term that is used in this thesis to describe the frequency range at which an amplifier properly function is its 'operational frequency'.

Like the frequency bandwidth, amplifiers have a limited range of allowed input power that will yield a useful output. This range is called the dynamic range of an amplifier. An ideal amplifier's output would follow the input linearly, however in reality after a certain input power the amplifier's output signal will no longer increase in power. When this happens the amplifier is saturated, and if the input power continues to be increased, it can permanently damage the amplifier.

2.7.1 Noise

In all electronic circuits there exists noise. Noise can be caused from several sources, a few of which are stated here. Thermal noise is caused by thermal motion of electrons, and is also called Johnson or Nyquist noise [34]. This noise is present in all components, and - as expected by it's name - is dependent on the temperature of the device. This noise can be

measured as the random changes in voltage over a given time. In a given frequency band, Δf, the time averaged noise voltage is given by

$$\langle u^2(f) \rangle = 4k_B T R \Delta f \,, \tag{2.24}$$

where T is the temperature of the device, and R is the resistance. As we can see, at absolute zero the thermal noise approaches zero. Flicker noise, or $1/f$ noise, occurs within almost all electronic devices. In reality the flicker noise can be expressed by $1/f^{\alpha}$ where α can vary between different devices, and within the same device. Furthermore it has been shown that $1/f$ noise can have temperature dependence. Quantum noise comes from the quantized nature of electrons and photons. It is usually the lowest level of noise in a system.

The noise floor is the sum of all noise in the system. The noise floor can be reduced by integrating over longer periods of time, expect for the $\frac{1}{f}$ component.

Noise Temperature

If a noise source is "white", or does not depend on frequency, one can calculate the equivalent noise temperature, T_e, of the source. Noise temperature is defined such that, if a device, outputting a noise of N, in Watts, was replaced with a resistor, R, then the noise temperature would be the equivalent temperature that the resistor would need to be at such that the Johnson-Nyquist noise (2.24) from the resistor was also N. T_e can be calculated by

$$T_e = \frac{N}{k_B B} \tag{2.25}$$

where B is the bandwidth of the component or the system. T_e is a useful number to know for microwave circuits to determine how much noise will be added to the system by the inclusion of the device.

For an amplifier, the noise temperature is a figure of how much noise is being added to your signal by the amplifier. To better understand this figure, consider a resistor at zero Kelvin at the input of an amplifier. The input noise to the amplifier would be zero, however the amplifier would have some internal noise, so that the output noise would be

nonzero, N_{out}. The described system would be equivalent to a noiseless amplifier with a resistor of temperature T_e connected to the input. T_e can be calculated by

$$T_e = \frac{N_{\text{out}}}{G k_B B} \tag{2.26}$$

where B is the bandwidth of the amplifier, and G is the amplifier's gain.

Amplifier Chain

While a single amplifier will add a noise value of N_0, for a chain of many amplifiers each amplifier does not add their full noise value. Rather, amplifiers connected in series will have a total noise output of

$$N_0 = (G_1 G_2 \dots G_n)\, k_B B \left(T_0 + T_{e1} + \frac{1}{G_1} T_{e2} + \cdots + \frac{1}{G_1 G_2 \dots G_{n-1}} T_{e\,n} \right) \tag{2.27}$$

where G_n is the gain, in dimensionless units, provided by the n^{th} amplifier in the series, T_0 is the input noise temperature to the amplifier chain, and T_{en} is the noise temperature of the n^{th} amplifier.

From this equation it ca be seen that the noise temperature from the first stage amplifier, T_{e1}, contributes the most amount of noise out off all amplifier noise temperatures. For this reason, it is good practice for the first stage amplifier to have the lowest noise temperature.

Signal to Noise Ratio

The signal-to-noise ratio (SNR) of is the ratio the signal power, P_{s}, compared to the noise floor, P_{n}, and is expressed by

$$\text{SNR} = \frac{P_{\text{s}}}{P_{\text{n}}}\,. \tag{2.28}$$

SNR is used to classify how much signal a measurement generates above the noise floor of the experiment.

Noise Figure

Another characterization of the noise of an amplifier is the noise figure, F. F represent the degradation in the SNR as the single passes through a device. The noise figure is the ratio of the input SNR to the output SNR

$$F = \frac{S_i/N_i}{S_o/N_o}\,, \tag{2.29}$$

where S and N are the signal and noise, in dimensionless units, and the subscripts i and o stand for input and output, respectively. For all amplifiers, there will be excess noise added by the amplifier ($N_o > N_i$) causing$F > 1$.

F is given in unit-less numbers; this value of noise figure can be converted to a united value of noise figure, NF, by

$$NF = 10\log_{10} F[\text{dB}]. \tag{2.30}$$

The noise figure can be converted to noise temperature - and vice versa - by the equation

$$T_e = (F-1)T_0\,, \tag{2.31}$$

when $T_0 = 290\,\text{K}$.

2.7.2 Types of Noise Temperature Amplifier Measurements

In order to determine some of the above listed amplifier characteristics, one needs to characterize the amplifiers. Following are three methods that can be used to measure the noise temperature of a device. Each method has advantages and disadvantages.

Y-Factor Measurement

A common way of measuring the noise temperature of a system is by the Y-Factor method. This involves changing the input noise to an amplifier, or amplifier chain, between two known noise sources of different noise temperature, T_{hot} and T_{cold}, as indicated in Figure

2.16. This can be done by either using a matched resistor at a known temperature, or a calibrated noise source.

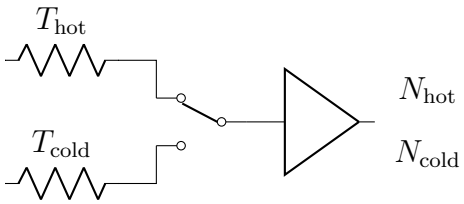

Figure 2.16: Basic diagram for a Y-Factor measurement. The input temperature to an amplifier is switched between a "hot" and "cold" resistors or noise sources.

From the measured output noises, N_{hot} and N_{cold}, the Y-factor term is defined as

$$Y = \frac{N_{\text{hot}}}{N_{\text{cold}}}\,, \tag{2.32}$$

which can then be used to calculate the noise temperatures of the system by

$$T_e = \frac{T_{\text{hot}} - Y T_{\text{cold}}}{Y - 1}\,. \tag{2.33}$$

An advantage of this measurement is that the gain (and losses) of the amplifier and rf signal pathway are not necessary to know to calculate T_e.

As mention above, there are multiple methods of making a Y-factor measurement, and we will explain two common examples: using a calibrated noise source, and using a resistor reference.

Calibrated Noise Source Y-Factor

A calibrated noise source outputs a defined Excess Noise Ratio (ENR) given by

$$ENR = \frac{T_S^{\text{on}} - T_S^{\text{off}}}{T_0} \tag{2.34}$$

which is usually frequency dependent. For a calibrated noise source, there are two common output ENR values, a high output of 15.6 dB, and a low output of 6 dB. Using such a noise

source, the Y-factor is given by

$$Y = \frac{N^{\text{on}}}{N^{\text{off}}}\,, \tag{2.35}$$

where $N^{\text{off(on)}}$ is the output noise with the device off (or on). Then noise temperature can the be calculated by equation 2.33.

This method can have the advantage that, when properly calibrated, the input noise to the amplifier is very well defined. However, for amplifiers that have a limited dynamic range, care must be taken to not overload the amplifier.

The disadvantages of the calibrated noise source method are a few fold. First, the operator lacks control to alter the input noise to the device; at cryogenic temperatures the input noise to the device will be determined by the attenuation in the rf input line and the physical temperatures of the attenuators.

A second and potentially larger issue with the calibrated noise source method is that there can be an impedance mismatch between the noise source and the device input. This impedance mismatch results in a relection of the singal at the input. It is paramterized by the Voltage Standing Wave Ration (VSWR),

$$VSWR = \frac{1 + |S_{11}|}{1 - |S_{11}|}\,. \tag{2.36}$$

S_{11} is the return loss. Ideally, $S_{11} = 0$ and so the $VSWR = 1$. The SQUID input impedance is not well defined but can be about 20Ω. Furthermore, this mismatch has a more pronounced effect when using a noise source with a large ENR when measuring a device with a low noise temperature [23].

Heated Resistor Y-Factor Method

A resistor of known temperature can also be used as a noise source. The resistance is typically matched to the amplifier's input impedance. The resistor is thermally decoupled from the amplifier and has its own heater and temperature sensor. By altering the temperature of the resistor, the operator can control the thermal noise (equation: 2.24), generated by the resistor. From changing the input noise, equations 2.32 and 2.33 can be used to

calculate T_e. An advantage of this method is that multiple values of the input noise can be applied to better calibrate T_e.

This method also has potential disadvantages. If the resistor is not properly thermally isolated from the amplifier, increasing the resistor temperature dramatically away from the amplifier temperature can cause the amplifier to warm up. Experimentally, we found achieving this level of isolation to be challenging on the ADR, because the system does not have the cooling capacity to keep the device at a sufficiently low temperature when the resistor temperature is high enough to measure a significant difference in input noise.

SNR Method

Another method is to measure the SNR and concert it to T_e. This method may seem the most direct way of determining the noise temperature of a device, however the dominant error occurs from the accuracy of the resolution bandwidth of the spectrum analyzer used to record the data. Furthermore, this method becomes more complicated due to the loss factors in the rf path that effect the SNR.

Chapter 3

Setup and Characterization of the Adiabatic Demagnetization Refrigerator

The goal of this project was to construct a testing cryostat to make low temperature measurements of various devices. For our cryostat, we used a High Precision Devices (HPD) SHASTA 106, which includes a Cryomech pulse tube cooler and an ADR, which provides a resting base temperature of roughly 2.7 K and an absolute base temperature in the 50-100 milliKelvin range. This section outlines the modifications we made to the system, and potential future work for further cryostat optimization.

3.1 Carbon Fiber Support System

The amount of entropy, and therefore heat, that an ADR can remove from a system is finite. The unmodified ADR's cold fingers, which are supported by Kevlar threads, can only support a limited mass ($\approx$ 1 lb), ideally with no torque as to not break or stretch the threads or cause a thermal touch. To allow for more weight to placed in the system we built a support structure that was physically attached to the pulse tube cooler's base

plate. We had two main requirements for this structural modification: that it had a low thermal conductivity, so that the minimal amount of excess heat flows from the pulse tube cooler into the sample stage of the ADR, and because this is a support structure, that the material be strong.

A previous group member, Shuchao Meng, initiated the design and constructions of a support system, in which a carbon fiber shaft taken from a X-Jammer-27^{TM} PRO archery arrow was used as the cryogenic supporting material. These shafts were chosen because of their cylindrical nature, small cross section, and structural rigidity. The hollow rod has the highest elastic section modulus out of many commonly used construction shapes, and its thin walled nature is ideal for low heat transfer between stages. The specific shaft used has an outer diameter of 10.42 mm and a wall thickness of 0.44 mm. We installed the system in the ADR system, as seen in Figure 3.5a. In order to confirm that this carbon fiber arrow shaft would satisfy our criteria for the support structure, its thermal conductivity, bending stiffness, compression rate, and electrical resistivity were measured. Altered arrow shafts were also tested to determine how removing material affected those properties.

The work presented in this section on measuring the thermal conductivity and other physical properties of the carbon fiber shafts presented in this chapter, was undertaken by Erin Tonita, Jan Kycia, and myself, and was published in reference [33]. Erin Tonita helped with the mechanical portion of the characterization of the carbon fiber shafts, and Jan Kycia suggested what thermal and mechanical characteristic should be measured as well as technical support during the measurement process.

3.1.1 Thermal Conductivity of Carbon Fiber Shaft

To quantify the efficacy of the carbon fiber shaft system as a thermal insulator, we measure the thermal conductivity of the carbon fiber shaft. For this measurement, two copper bands were placed around a piece of the arrow shaft 3.43 cm apart and each band was connected to a RuO_2 thermometer [24] via GE varnish. The RuO_2 thermometers were connected to our readout with four 6μm diameter NbTi wires, selected to ensure that the thermal conductivity between the resistors and the rest of the wiring would be much less than the thermal conductivity of the shaft. One end of the arrow shaft was thermally anchored to

the cold stage of the ADR via clamping it to a copper block, to act as a heat sink, and a 20 kΩ resistor was attached to a copper band at the free floating end of the shaft to act as the primary heater. A radiation shield was placed around the entire configuration and heat sunk to the cold stage of the ADR. Calibration of the RuO_2 thermometers was achieved on a separate cool-down by shorting the Cu bands with a wire to the cold stage of the ADR and measured against a calibrated GRT. Readout of the thermometers was done by a Lake Shore 370 AC resistance bridge. This method of thermal conductivity measurements is described in section 3.3.8 of reference [34].

The thermal conductivity coefficient, κ, was then calculated by

$$\kappa = \frac{qL}{A\Delta T}\,, \tag{3.1}$$

where q is the applied heat at one end of the arrow shaft, ΔT is the difference in recorded temperature between the two thermometers, and L and A are the length between the two thermometers and the cross-sectional area of the carbon fiber shaft, 3.43 cm, and 0.13 cm^2 respectively. Using the magnet on the ADR, we were able to hold the cold stage at a constant temperature, then we varied the applied voltage to the resistor to set q such that ΔT between the RuO_2 thermometers ranged from 10% to 20%. The results of the test can be seen in Figure 3.1.

The results were compared to values of other cryogenic insulating materials[36], such as Graphlite, G10, and Vespel SP-1. The measured data was fit to the formula, $\kappa(T) = \alpha T^{\beta}$, yielding values $\alpha = 8.8 \times 10^{-5}$ [W/(cm K)], and $\beta = 1.54$. These tests indicate that this carbon fiber composite shaft is a thermal insulator comparable to several other cryogenic support materials. To our knowledge, achieving this aspect ratio is unique to carbon fiber, and is not achievable with other materials listed with similar strength characteristics.

However, the measured thermal conductivity is higher by a factor of roughly 4 than the reported thermal conductivity of epoxy-free carbon fiber as measured by Nicholls *et al.*[31]. We attribute the difference in thermal conductivity to the epoxy, used in binding the carbon fiber weave, being the dominate source of heat transfer at low temperatures.

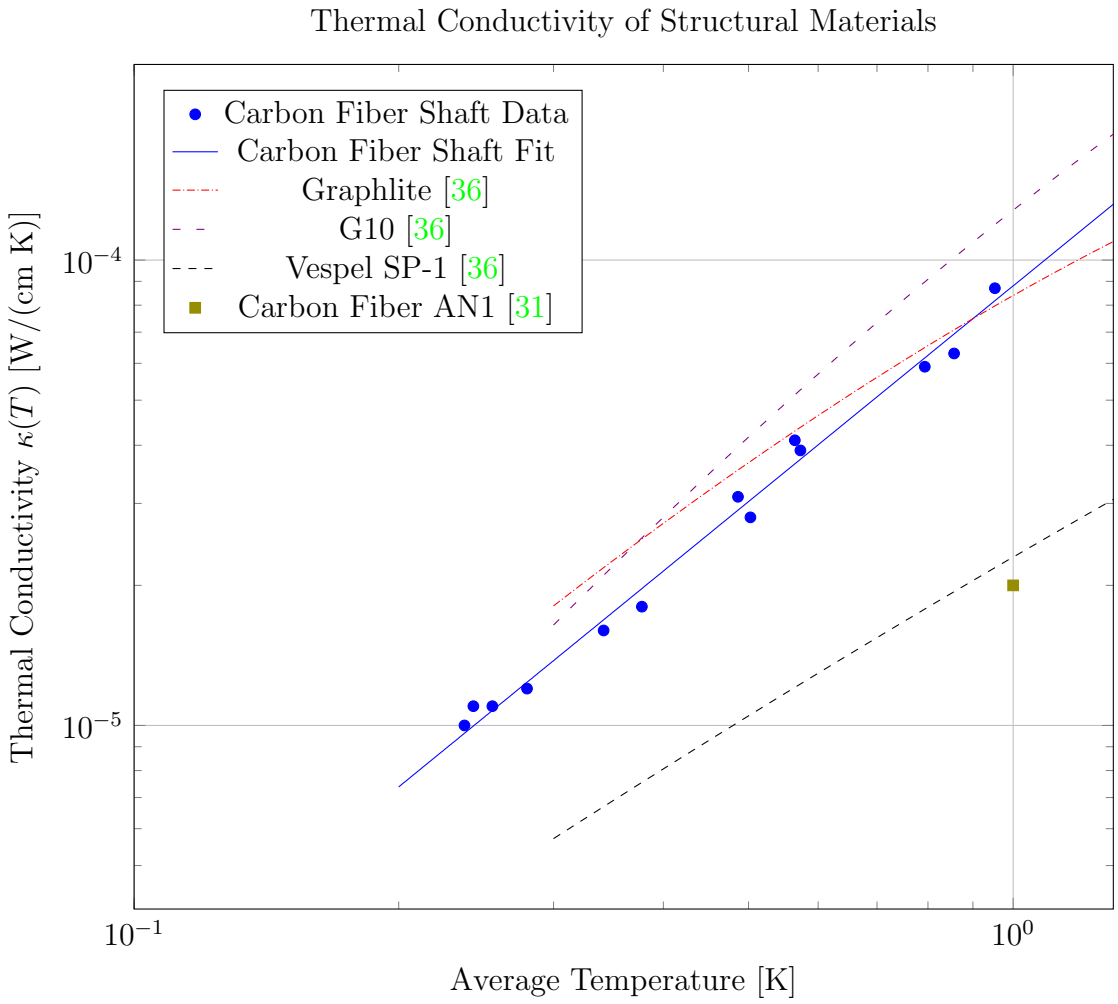

Figure 3.1: Measured thermal conductivity of the arrow plotted against other cryogenic support materials. Data from Runyan *et al.*[36] valid to 300 mK.

Electrical Properties

To examine other electrical properties of the shaft, we used the setup used for the thermal conductivity measurements to make a 4-wire resistive measurement over the small shaft sample, after adding copper wires wrapped around the shaft and bonded to the sample with silver paint. Results show that the material is a good conductor in all temperature ranges

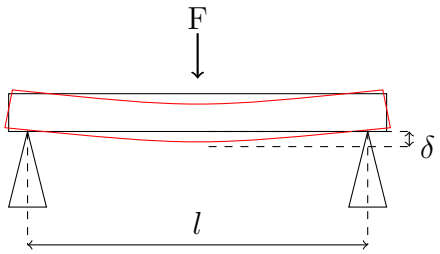

Figure 3.2: Diagram of a 3 point flex test.

with a resistance of 0.018 Ω and 0.044 Ω at room temperature and 200 mK respectively, and that the resisitivity of the sample increased monotonically from 300 K to 200 mK, indicating that the carbon fiber shaft does not follow Wiedemann-Franz Law.

3.1.2 Structural Strength of Carbon Fiber Shaft

While we knew, empirically, that the shafts were strong enough to support the load of a normal sized experiment, we wanted to further test their physical properties. The shaft's bending stiffness and spring constant were measured to determine its structural strength.

The bending stiffness, defined by

$$\text{Bending Stiffness} = \frac{l^3\, F}{\delta} \tag{3.2}$$

was measured by performing a 3-point flex test (see Figure 3.2), where F, was the force applied to the shaft's center, l, was the length of the shaft, and δ was the measured deflection of the shaft.

The spring constant,

$$\text{Spring Constant} = \frac{F}{\Delta l} \tag{3.3}$$

of the shaft was also measured, where Δl was the measured change in length of the shaft, as a force, F, was applied along the vertical axis. Efforts were taken to reduce the amount of bowing by the samples by placing the shafts in a loose fitting cylinder. Results of these tests can be found in Table 3.1.

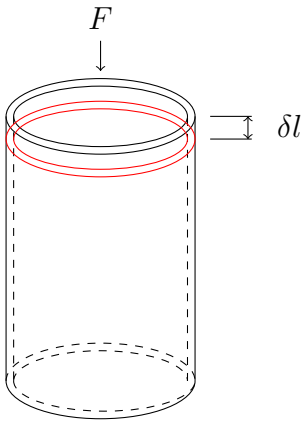

Figure 3.3: Diagram of the compression test.

From the spring constant test (seen in Figure 3.3) on the shaft, we can determine the Young's modulus, E, value of the carbon fiber shafts by the following equation

$$E = \frac{l_0}{\delta l}\frac{F}{A}\,, \tag{3.4}$$

where δl and l_0 are the amount the shaft was compressed and the initial length, respectively, F is the applied force to the shaft in the vertical direction, and A is the cross-sectional area of the arrow shaft. The calculated value of E is 18.2 GPa. This value is less than the reported carbon fiber value of 69 GPa–150 GPa from the Materials Data Book for Engineers and Scientists[32]. This reduction of Young's modulus is not unexpected because the specific type and orientation of carbon fiber weave, along with the weave to epoxy ratio, used in this arrow shaft is unknown.

3.1.3 Reduction of Carbon Fiber Material

During the construction of the carbon fiber shaft support structure, it was discovered, as well as experimentally verified, that the full carbon fiber shafts more than met the structural requirements of the system. Portions of the area were machined away, with two different patterns, to test if the thermal properties of the shaft could be reduced without significantly degrading the structural integrity of the support structure.

The first pattern was designed to maximize the length of heat flow from the ends of the shaft, and the second pattern was designed to increase the structural strength by ensuring that all triangle patterns shared verticies. A sketch of the two different machining patterns can be seen in Figure 3.4, along with labels explaining the naming convention we used.

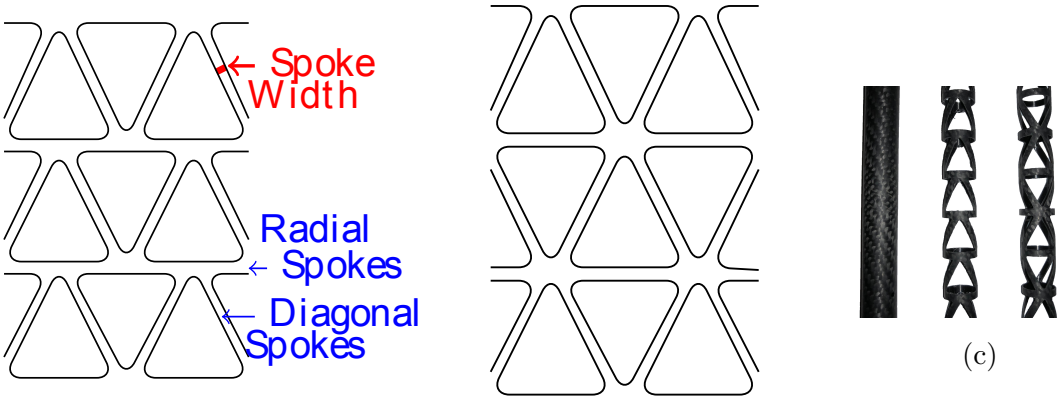

Figure 3.4: (a) The first machining pattern tested. Designed to maximize the length of heat flow. (b) The second machining pattern. Designed for more structural support. Width of the diagonal spokes were used as the variable to determine how much material to remove. (c) A photo of an unmachined carbon fiber shaft along with first (center) and second (right) machined carbon fiber shaft.

Structural Strength

The bending stiffness and spring constant was measured for both machined shaft configurations. Various amounts of materials were removed by altering the spoke width (illustrated in Figure 3.4). Results of these tests can be seen in Table 3.1.

We found that the machining did significantly reduce the structural strength of the shaft, however if the spoke widths are a medium grade - roughly 2 mm - we believe that they can be incorporated into a design without excessive loss of strength. For lighter experiments, that need to be highly thermally isolated, a long shaft with a thin spoke width can be used. For example, during the spring constant testing for the second machined

Arrow Machining Pattern	Spoke Width [mm]	Bending Stiffness $[\mathrm{Nm}^2]$	Spring Constant for 20 cm of shaft [N/m]	Reduction of Bending Stiffness	Reduction of Spring Constant
Full Shaft	-	243	1.2×10^6	1 x	1 x
First	2.84	15	2.7×10^5	0.062 x	0.225 x
First	2.07	2.7	1.7×10^4	0.011 x	0.014 x
First	1.32	0.35	2.8×10^3	0.001 x	0.002 x
Second	2.22	3.18	1.0×10^5	0.013 x	0.083 x
Second	1.26	0.58	3.5×10^4	0.002 x	0.029 x

Table 3.1: Physical properties of X-Jammer-27$^{\mathrm{TM}}$ PRO shaft before and after machining portions of material away in two different patterns

pattern, with the spoke width of 1.26 mm, the shaft was still able to support 1 kg without breaking.

Thermal Properties

Thermal properties of the machined shaft were also calculated for the machined shafts. As stated in 3.1.2, the thermal conductivity of the shaft is most likely dominated by the epoxy. We assumed that the thermal conductivity is isotropic despite the anisotropy of carbon fiber in thermal conductivity. This allowed us to calculate of the thermal resistance of the arrows after machining, using the width and length of both the diagonal spokes, as well as the width and length of the radial sections. The thermal resistance of each component given by

$$R_\lambda = \frac{1}{\kappa(T)} \frac{l}{w\,t} \tag{3.5}$$

where $\kappa(T)$ is the measured thermal conductivity, and l, w, and t are the length, width, and thickness of the two types of sections. This gives $R_{\lambda,\text{ spokes}}$ and $R_{\lambda,\text{ radial}}$, from which one can sum up the thermal resistances in the machined pattern to calculate total thermal resistivity, as reported in Table 3.2.

Because the material is unchanged under machining, any change of the specific heat will be due to the reduction of mass. Therefore, the difference of mass, from the machined sample to the non-machined sample, was measured, and the ratio was reported as the reduction of specific heat, which is also listed in Table 3.2.

Arrow Machining Pattern	Spoke Width [mm]	Thermal Resistance for 20 cm of shaft [K/W]	Increase of Thermal Resistance	Reduction of Specific Heat
Full Shaft	-	$1.7 \times 10^6\, T^{-1.54}$	1 x	1 x
First	2.84	$4.9 \times 10^6\, T^{-1.54}$	2.9 x	0.63 x
First	2.07	$7.8 \times 10^6\, T^{-1.54}$	4.6 x	0.38 x
First	1.32	$1.4 \times 10^7\, T^{-1.54}$	8.2 x	0.25 x
Second	2.22	$6.2 \times 10^6\, T^{-1.54}$	3.6 x	0.37 x
Second	1.26	$1.3 \times 10^7\, T^{-1.54}$	7.7 x	0.25 x

Table 3.2: Thermal properties of X-Jammer-27$^{\text{TM}}$ PRO shaft before and after machining portions of material away in two different patterns.

3.2 Heat Load and Hold Time of the ADR System

For a cyrostat without constant cooling power, it is important to consider the hold time of the system. This determines what types of measurements that can be made. The hold time is defined as how long a system can stay at, or below, a constant temperature. Manufactures typically quote the hold time for ADRs at 100 mK. For a non-continuous cryostat, the cooling capacity is also reported, which is the amount of energy that can be removed from the system at the given temperature. From the manufacture's website, the SHASTA 106 ADR has a hold time of $120 - 250$ hour, when there is no load on the system [14]. While most types of experiments will add additional heat to the system, and therefore effect the hold time, it is important to look at the intrinsic heat load on the system and determine which components are the dominant contributing factors. Our system has four

major stages: the pulse tube cooler stage which is roughly at 2.7 K, the GGG stage which is thermally anchored to the GGG salt pill and is nominally at 1 K, the intermediate cold stage which is thermally connected to the FAA pill and is the coldest part of the system with an ideal base temperature of 50 mK, and the sample stage which has a weak thermal link to the FAA stage. Heat can be introduced into the cold stage from several sources. In the following section we will take a look at four main sources of heat: heat flow due to physical connections to the cold stage from higher temperature regions via the support structure, electric wiring, and rf coaxes as well as heat from black-body radiation.

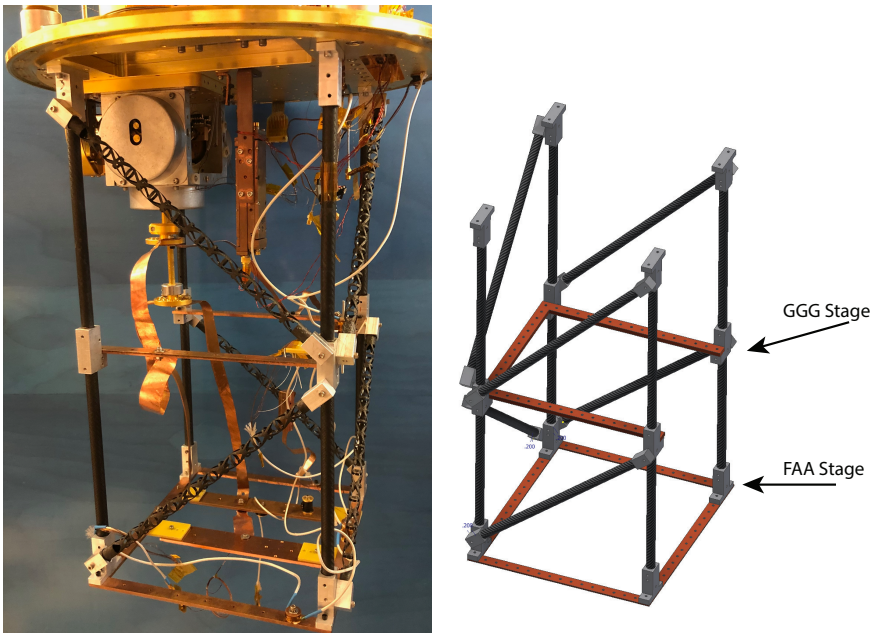

(a) (b)

Figure 3.5: An image (a) and a rendering (b) of the current support structure of the cryostat. The diagonal legs of the structure have been replaced with the machined version of the arrow shafts, which is not depicted in the rendered version.

3.2.1 Carbon Fiber Legs

The heat load on the ADR is greatly affected by the carbon fiber support structure, as it provides the most massive and direct path from the cold stage to the base of the pulse tube cooler. As described, a multilevel support structure was designed and built, a picture and rendering of which can be seen in Figure 3.5. In this design, there is a heat leak from the pulse tube stage to the copper band that is thermally connected to the GGG cold finger, nominally at 1 K, As well as a heat leak from the GGG stage to the lower copper band which thermally connectes to the FAA cold finger. The DUT is nominally thermally anchored to the base stage. Figure 3.5b shows a diagram of the copper parts of the support structure, as well as labeling the different stages. The purpose of the multilevel design was to allow heat sinking at several stages, thereby reducing the heat flow to the DUT. While these heat leaks are unavoidable, design choices can be made to minimize heat flow.

The number of legs, and their length, are a large factor in determining the heat flow between stages. Currently each stage is separated by 22.86 cm (9"), however when calculating the heat flow the effective length of the arrow rods must be taken into consideration, where the reciprocal of the effective length is given by the summation of the reciprocal of each individual component. The effective length of the support structure for heat flow calculations is then 3.16 cm (1.2 in). Increasing the effective length would be an effective way to decrease the heat load on the low temperature legs.

As shown in section: 3.1.3, another way to reduce the heat load is to machine portions of the legs away. Machining with the correct pattern would reduce the thermal conductance by roughly a factor of four. However, one must be careful not to reduce the physical strength of the arrows to a point where they could not support the weight of the structure, any supporting electronics, and the DUT.

Connection Material

Another factor that needs to be considered when designing and deploying the support structure are the properties of the materials used that connect the carbon fiber shafts to each other and to the rest of the apparatus, as connection from the carbon fiber shafts

directly to either the pulse tube cooler base plate or the low temperature stages is not practical. In the current design, aluminum blocks were used as the connecting material. Aluminum was chosen because it is easy to machine, light, and plentiful. Obviously, the pulse tube cooler must cool down this extra material as well, therefore an ideal support design would add as little material as possible, and the added material would have a low specific heat. It takes about 19 mJ of energy, almost 20% of the FAA stages total cooling capacity, to cool down the amount of aluminum used in the system described in this thesis.

3.2.2 Coaxial Cables

RF coaxial cables (CC), commonly referred to as coax(es), are necessary to perform any measurements that require frequencies above a few hundred hertz. A coax consists of an inner and outer conductor, separated by a dielectric material. The heat flow through the coax will depend on which metal is used as the conductor, as well as on the form factor of the cable. Coaxes can come in many different sizes, and where the thinner diameter coaxes will have a lower thermal conductivity, due to the smaller cross sectional area, they suffer from greater attenuation at higher frequencies. At low temperatures, it is common for the conductor to be made from superconducting material for the reasons discussed in section 2.4.

In the cryostat used for the work presented in this thesis, 085/50-NbTi coaxial cables were used with an outer diameter of 2.159 mm (0.085") and an impedance of 50 Ω. A single piece of NbTi coax was used between the pulse tube cooler plate and the FAA stage, where it was thermally connected to each stage at both ends, as well as thermally connected to the GGG stage in the middle of the coax.

3.2.3 Wiring Heat Load

Electrical wiring is necessary to measure the various aspects of any experiment, however the introduction of such wiring introduces another source of heat. To minimize the added heat, it is common, in low temperature experiments, to use superconducting wiring. As previously mentioned, the thermal conductivity of a superconductor is much lower than a

normal metal, therefore superconducting wires are ideal for low temperature experiments. To further minimize the heat flow to the DUT, heat sinking is implemented at two stages, for each the wires were heat sunk by wrapping them tightly around a copper bobbin which was then heat sunk to the temperatures stage. The first stage of low temperature heat sinking is achieved at the GGG stage and second is heat sunk to the FAA stage, where they are then connected to the device or sensor. By heat sinking the wires to the FAA stage before connection to the sample stage, we can reduce the thermal load on the sample while only slightly increasing the thermal load on the FAA stage.

We used NbTi wires with a diameter of roughly 0.005" in our experimental setup. If we connected 25 wires with a length of 30 cm from the pulse tube cooler to the GGG stage, and then had another 30 cm to the FAA stage we would expect a thermal load of $1.5 \times 10^{-1}\,\mu$W and $7.41 \times 10^{-3}\,\mu$W of heat on the GGG and FAA stage respectively. The heat load due to the wires are on the same order of magnitude as the heat from the coaxes, and are an order of magnitude less than the heat due to the support structure.

3.2.4 Radiative Heat Load

The cryostat has a radiation shield connected to the pulse tube cooler stage, meaning the entire cold stage is being bombarded by black-body radiation at 2.7 K, which is equivalent to $2.608\,\mu\mathrm{W}m^{-2}$. However, because both cold stages are made of polished copper, their emissivity is low enough, 0.025, that effectively only the radiation heat absorbed by the support legs needs to be considered. Because the legs are made of black carbon fiber, we assume that they have an emissivity of 1. For calculation purposes, we further assume that each leg can be considered a single lumped element, where all radiation is absorbed, and that heat flows equally to each end of the legs (as illustrated in Figure 3.6), where we are assuming that $R_{\mathrm{thermal}_1} = R_{\mathrm{thermal}_2}$.

3.2.5 Heat Load Analysis

To calculate the total hold time of a system we can look at the four main heat loads on the GGG and FAA stages as discussed in sections 3.2.1 - 3.2.4, the carbon fiber support

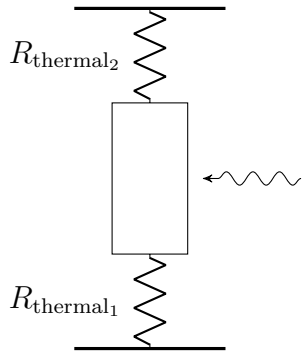

Figure 3.6: Illustration of the heat flow in the carbon fiber shafts due to radiation.

legs, wiring, coax input and outputs, and black-body radiation. The heat load of each component was calculated and related to the reported heat cooling capacity of the ADR; the results of this calculation can be seen in Table 3.3.

	$\dot{Q}$ GGG stage [W]	$\dot{Q}$ FAA stage [W]
Carbon Fiber Support	8.8×10^{-6}	7.7×10^{-6}
25 Wires	1.5×10^{-7}	7.4×10^{-9}
4 Coaxes	2.6×10^{-7}	5×10^{-7}
Radiation	1.2×10^{-7}	6×10^{-8}
Calculated Hold Time	35 hours	4 hours

Table 3.3: Calculated heat loads of four major sources of heat on each stage of the ADR system along with total hold time calculations.

The calculations were made with the following assumptions.

- 25 NbTi wires of a diameter of 0.005" and the wires have a length of 30 cm were used between each stage.
- Four NbTi coaxes of length 22 cm were used between each stage.
- The thermal radiation is absorbed by a single lumped element, and the heat flow is split evenly between the ends of the arrow shaft.

Therefore, we expect the hold time of the ADR setup to be approximately 4 hours, however in practice the actual hold time, at 100 mK, is about 1 hour.

3.3 Further Plans for Heat Load Reduction

As currently presented, the ADR system functions with the carbon fiber support system laid out in the preceding section. However, by further optimizing and reducing the heat load, we can facilitate measurements that require longer times at the sub 100 mK range. The following section outlines future work that could be implemented to improve the hold time of the ADR system.

3.3.1 Modification to Carbon Fiber Legs System

As we can see from Table 3.3, the dominant contribution to the heat load comes from the carbon fiber support legs. This can be addressed in two different ways.

As mentioned, the heat conducted for each legs is inversely proportional to the length. Preliminary work has gone into designing a new leg support structure that uses only diagonal legs to increase the effective length. However this has not been implemented. Initial calculations show that using six diagonal legs, instead of the current set up, would reduce the thermal conductivity by about a factor of slightly better than two.

Replacing the aluminum blocks is also a priority. A few different materials were considered as a replacement: Cu Pb, Sn, and Torlon. A plot of the specific heat of these materials can be seen in Figure 3.7. As mentioned, the goal is to select a connection material which minimizes the amount of energy necessary to cool the material. The specific energy of the considered materials, in the temperature range from 0 K to 2.8 K, is presented in Table 3.4. Of these materials, copper, has the smallest specific heat in terms of volume. While aluminum does have a small heat capacity per volume value, the increase due to the superconducting transition is a noticeable effect during our cooldown. Because the ADR has more cooling capacity when the field is higher, we would rather have the trade off of high

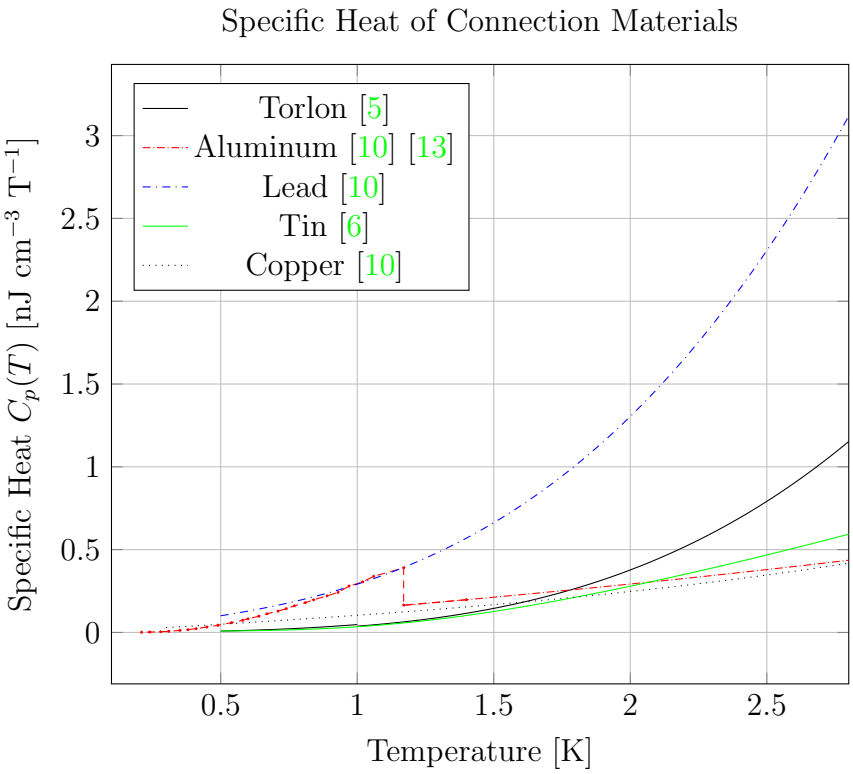

Figure 3.7: Specific heat of different materials considered for connection at low temperatures.

of larger heat capacity at higher temperatures. For these reasons, we suspect tin or copper to be a more ideal element than aluminum for the connection pieces.

Material	Specific Energy [μJ cm^{-3}]
Torlon	0.00075
Al	0.00062
Pb	0.0025
Sn	0.00083
Cu	0.00048

Table 3.4: The specific energies of the material presented in Figure 3.7

The specific heat of most materials drops considerably at lower temperatures. It follows that the lower the temperature that the pulse tube cooler can reach, the less energy it will take to remove heat from the materials. Copper, Torlon, and tin have comparable specific heats by volume around 1 K and below. If a 1 K pot were to be used to reduce the temperature of the system, then the heat load on the salt pills from the connection materials would be significantly reduced.

3.4 Operating the ADR System

We set out to automated the system and implement modifications to allow for remote control capabilities. If the ADR could be controlled from anywhere and measurements could be automated, downtime of the system would be drastically reduced. To that end, the following section describes the operation of the ADR, and additions that we have made that allow easier use of the cryostat and allow for remote operation.

3.4.1 Pulse Tube Cooler Alterations

As previously explained in section 2.3, the ADR has two primary cooling methods. The first method is the pulse tube cooler, and apart from altering the amount of helium gas in the system, no further work went into improvements of the system. The amount of helium in a pulse tube cooler affects the cooling ability of the cryostat. Ideally, the amount of gas in the system will cause the pressure in the reservoirs to be such that there will be a phase shift betwen the flow of gas and temperature flow. We varied the amount of gas in the reservoir and observed that reducing the volume of the gas also decreased the temperature of the pulse tube cooler, however this also decreased the cooling power; the inverse also held true. We tuned the amount of helium in our system so that the pulse tube cooler would have a base temperature of 2.68 K.

The pulse tube cooler must be manually turned on, and it takes 26 hours to cool the system from room temperature to its base temperature of about 2.6 K. This process could not be easily automated. It is recommended that the pulse tube reaches its base

temperature and is kept there for some time before use of the ADR, as the pulse tube cooler is still removing heat from all portions of the cryostat.

Cooling Procedure using the Adiabatic Demagnetization Refrigerator

The second cooling method is the ADR, and it is comprised of a superconducting magnet, heat switch, and salt pills. Control of the current through the magnet, as well as control of the heat switch was automated. A KEPCO BOP-20 was used to supply current to the superconducting magnet. We installed a General Purpose Interface Bus (GPIB) interface card into the KEPCO to allow for computer control. The KEPCO can be operated in either a current mode or to a voltage mode. When in voltage mode, the device will output the desired voltage until either the hard set current limit, or the programmed soft current limit, is reached; when in current mode, the device will attempt to output the desired current while altering the voltage. We can take advantage of the different modes to use the power supply in slightly different functions, depending on how we want the system to behave. Control of the KEPCO was done via a LabView program which I helped to write.

The first use of the program is to ramp the magnet. While in voltage mode, a soft limit of 10 A is programmed, and a desired output voltage, or ramp rate as it will be subsequently called, is used to slowly increase applied current to the magnet. This ramping procedure occurs when the heat switch is closed, thereby allowing the heat of magnetization to be removed by the pulse tube cooler.

After the magnet has been ramped to the desired current and the temperature has decreased to the level at which the ramp was started, indicating all heat from magnetization was removed, the heat switch is opened which thermally disconnects the salt pills from the pulse tube cooler. This can be done either by a 5 V pulse, provided by a BNC-DAQ 2090, or a manual switch on top of the cryostat. The ramp rate of the KEPCO is then set to a negative value, which causes the magnet to adiabatically demagnetize. The ramp down voltage is maintained until the desired temperature is reached, or the field in the magnet is reduced to zero. After either of those points have been reached, the ramping/de-ramping procedure is complete.

Magnet Temperature Control

During the ramp down process, the LabView program can be switched over to its second function, temperature control mode. In this second mode, the KEPCO is switched over to the current controlled mode. While monitoring a temperature sensor, the user can input a desired temperature, which instructs the KEPCO to output a current in attempts to keep the monitored temperature close to the desired temperature. If the physical temperature is above the desired temperature, then the current is decreased, and if the physical temperature is below the desired temperature, the current is increased. This method does not have a formal proportional integral derivative (PID) loop. Oscillations around the desired temperature can be seen. This could be reduced by introducing an integration time constant or lowering the effective proportional term. The with proper procedure keeping the temperature within 10% of the set temperature was achievable. The KEPCO will continue to vary the output current until programmed otherwise, or until there is no current left in the magnet at which point the KEPCO can no longer temperature control system.

3.5 Switching Network

In order to test multiple devices within a single cooldown, two Radiall R573423600 - effectively single pull six throw (SP6T) switches - were incorporated. The Radiall switches operate by activating a latching solenoid which raises (or lowers) a non-conducting rod, which in turn causes a gold conductor to break (or complete) the rf signal path to an output. A picture of the rf switches, along with labels of their components, can be seen in Figure 3.8. By staggering the switches, we can allow the signal path to pass through a maximum of six different devices. A diagram of a potential rf signal pathway can be seen in Figure 3.9.

Note that these switches are not true SP6T, because multiple solenoids can be activated simultaneously. When multiple solenoids are active, multiple outputs are connected to the input. This disrupts the impedance matching of the rf switch, causing reflection in the microwave circuitry. Therefore, we do not plan on using the switch as a way to split the rf input to multiple devices.

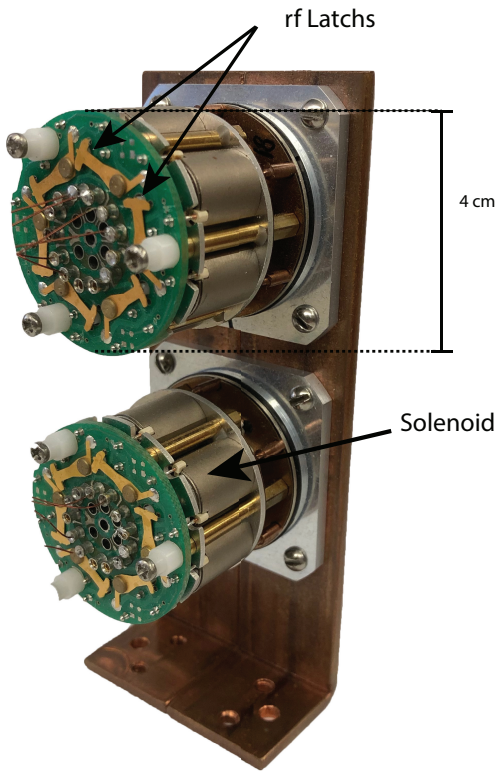

Figure 3.8: Image of the Radiall switches. The two switches are attached to a copper block to minimize their profile as well as thermally anchor the switches.

3.5.1 Modifications to Cryogenic rf Switches

Modifications were made to the Radiall switches to tailor their functionality to our setup The work presented in this section is based on documentations from the Martinis Group. The original design of the rf switches uses a "reset" switch which causes all six magnets to latch to the rf 'open' position. This modifications enable a coil to be toggled independently by sending a pulse of the opposite polarity to latch or delatch the switch. By controlling a single coil, we reduce the amount of power, therefore heat, necessary to disconnect an output from the RF pathway. Modifications to the physical switches consisted of removing the switches protective casing and manually removing sections of the wiring that caused the 'reset' pin to function. Figure 3.10 shows the circuit diagrams of the unmodified and

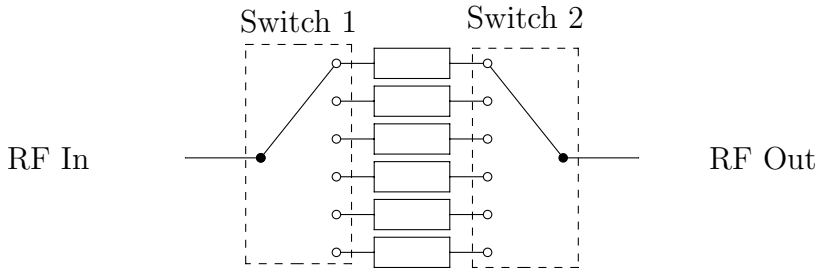

Figure 3.9: A diagram of a potential use of two cryogenic rf switches

modified circuits.

3.5.2 Room Temperature rf Switch Control Box

To power the solenoids, a supply pulse of 28 V must be applied to the actuators. In a room temperature environment this is easily achievable with a standard power supply. However, when the switches are in a cryogenic environment, applying a high voltage pulse for extended periods of time can dramatically heat up the switch and thermally connected areas due to the heat dissipation in the circuit. To reduce the heating, a custom switching box was built (see Figure 3.11 for a schematic). The design principle behind this box was to charge a capacitor to 28 V, which was then to be used to power the rf switch instead of a direct connection from a power supply. Because, in this design, only the capacitor can supply voltage to the rf switch, only a set amount of energy can be applied. This prevents an excess amount of energy to cause heat at the low temperature stage.

In this design, two double pull double throw (DPDT) switches are used to connect a capacitor to either a DC power supply of 28 V, or to the Radiall switch. The first switch (DPDT 1.X in Figure 3.11) in the series is the charge/discharge switch. When in the charging state, the power supply is connected to the resistor capacitor network in order to charge the capacitor. When switched to the discharging state, the ends of the capacitor are shorted via the Radiall actuator, which will cause the Radiall switch to activate. The second switch (DPDT 2.X) is an auxiliary switch that is used to determine the polarity of the pulse. By alternating the position of DPDT 2.X, we can control the direction of

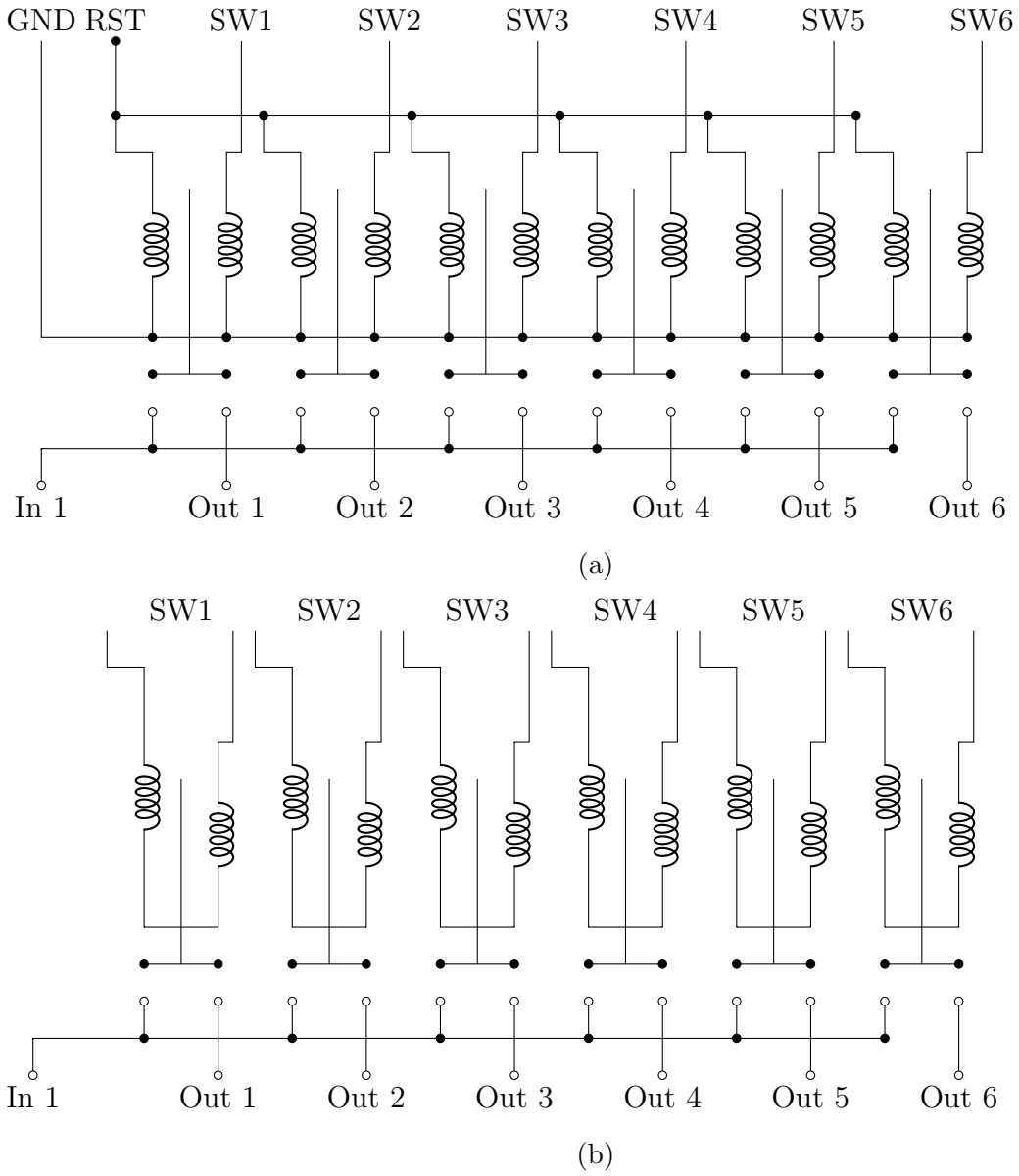

Figure 3.10: Circuit diagram for the (a) unmodified and (b) modified Radiall Switch. SW1-6 are electromagnetic solenoids that control actuators, which connect the RF input to a desired output shown on the bottom part of the circuit.

current flow, thus allowing the user to either latch or delatch a specific Radiall channel. Each instance of the described circuit can control one channel of the rf switch. Therefore, 12 instances are necessary for complete control of the Radiall switching network.

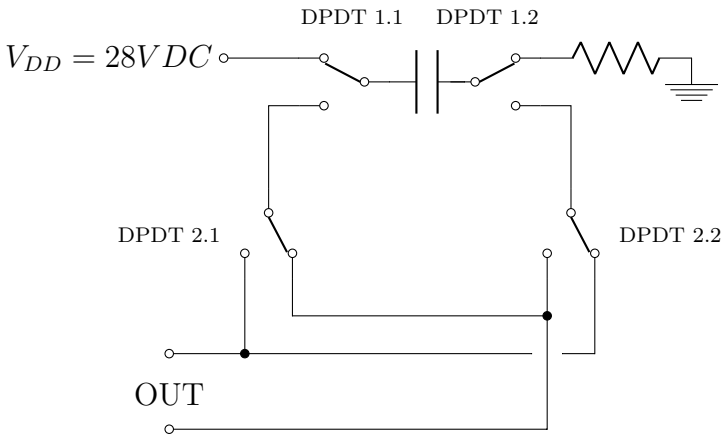

Figure 3.11: A circuit diagram for a single channel of the Radiall switch control box.

3.6 Automated Current Source

To further automate data collection, we designed, constructed, and implemented a computer controlled current source that could safely bias multiple MSAs, simultaneously. A portion of this work was conceived and completed at the University of Washington under Andrew Wagner and Leslie Rosenberg in the Axion Dark Matter Experiment (ADMX) group.

As noted in section 2.2, a I_{Bias}, and ϕ_{Bias} are necessary to operate an MSA. Because fluctuations of either I_{Bias} or ϕ_{Bias} can greatly impact the response of the SQUID, modern biasing devices are designed to keep these parameters as stable as possible, and have very low electronic noise. A standard biasing device is a precision voltage regulator, applied to one end of a variable voltage divider, which is usually controlled by a manual potentiometer. This basic principle was kept the same, however many of the components were replaced with their digital equivalent to allow for computer control.

3.6.1 Design Principle

The automated current source is divided into two separate boards. The board connected to the computer is called the "relay board", and the board that sources the current is called the "biasing board". While the entire system can be envisioned in three layers. The first layer is the individual integrated chips (ICs) and static components. This includes the several op-amps, resistors, capacitors, and specialized chips. The second layer is interfacing from the ICs to a central processor. The processor acts as the brain of the boards, telling what chip to execute what action. To communicate with the ICs, the user must send predefined inputs, which are specified by the chips. Lastly, the third layer is a computer program to interface with the central processor and to automate the processor commands. To interface with the ICs we used a microprocessor, an Arduino variant called a EtherTen, to communicate commands from a central computer to the chips. Commands to the EtherTen, from the computer, are written in MATLAB. However, any programming language that can interface with a server can be used.

The two boards communicate via fiber optics rather than an electronic connection. We did this so that the biasing board does not share an electronic ground with the relay board and computer system. This is because the experiment ground is filtered to minimize the noise, whereas the computer ground is connected directly to wall power which is known to be noisy.

Serial Peripheral Interface (SPI)

Because both boards use Serial Peripheral Interface (SPI) as a means of communication, a quick review of the SPI communication protocol will be presented. SPI is a way that several ICs can digitally communicate. SPI communication uses three or four digital input output (DIO) lines: Clock (CLK), Chip Select (CS), Master Out, Slave In (MOSI), and Master In, Slave Out (MISO). Communication is usually between a master (or controller), which is usually a processor that a user can program, and a slave (or minion) IC. The use of the term 'slave' in programming and IC inputs has, rightly, come under pressure. While the terms are still used at the time of writing, I will be adopting a different term 'minion'

to replace the term 'slave'. Normally the minion IC has a designed function, whereas the master IC can be written for any number of purposes. CLK, CS, and MOSI are necessary for the master IC to send commands to the slave IC, and the MISO line is only necessary if the minion IC needs to send information back to the master IC.

Under normal circumstances both the minion and master IC will operate on similar voltage rails. Standard terminology is that a voltage near the rails (usually 5 V), which is considered a 'high' signal, and a voltage near ground (0 V) called a 'low' signal. The basic SPI communication protocol between a master and minion is as follows. A master will alter the voltage of the CS line, so that a specific minion will become active. At this point, the minion will start to 'read' the input of the MOSI line. The master will then send a series of bits, low and high voltage pulses, to the minion via the MOSI line. After the command is sent (which can be a single byte or more) the CS line will be reverted to the original state, indicating to the minion that the full command is sent. Then the minion will process and execute the command sent by the master. If the command demands a response, the data will be sent via the MISO line the next time that the CS line is pulled active. The purpose of the CLK line is so that both ICs will be synchronized in their read write rate.

The advantage of SPI is that, while a minimum of three lines are necessary to communicate with the first IC, only one extra line is necessary for each proceeding IC. This is because all chips can operate connected to the same CLK, MOSI, and MISO lines; an IC will only 'listen', or process data, if its CS line is in the active state.

Note that this is only a very basic summary of SPI communication, and there are cases where the presented information here does not hold true. Furthermore, this is not the only way for processors to communicate with ICs; there are other communication protocols such as I2C. However, I2C is not used in the current design, because some chips used do not communicate via I2C. Introductary text, as well as programming guides, on SPIC, I2C, and digital communication can be found at online at Ref [18].

Relay Board

The relay board uses an EtherTen processor, which has built in Ethernet communication, as the central processor. The Ethernet communication allows for this board to connect to a computer network. With the EtherTen, the board can be programmed with a static Internet Protocol (IP) address, much like most standard scientific electronics, so that commands from a computer can be sent to the board. After programming the EtherTen a valid command can be sent from a user and and the EtherTen will convert that into a series of commands that the ICs on the current source board will understand. The commands will be sent to the current source board via a fiber optic network. A schematic of the board can be seen in A.2.

Current Source Board

The current source board digitizes a conventional SQUID bias box. A battery can be used to supply clean power to the circuit, which is then further regulated to the desired voltage with low drift voltage regulators. The board supplies current to the MSA(s) via two voltage dividers acting as inputs to a summing circuit. The two voltage dividers are implemented by using a two channel digital potentiometer, an AD5235. This chip has 1024 steps between each end of the divider. One advantage of this chip is that its logic levels can be either $+5\,\mathrm{V}$ and GND, or $+2.5\,\mathrm{V}$ and $-2.5\,\mathrm{V}$. By using the $\pm 2.5\,\mathrm{V}$ logic levels, we can supply either a positive or negative current. However, by making the digital potentiometers bipolar, we have introduced further complication into the circuit design by having two separate logic levels on the same board. Most ICs do not have the option to operate at $\pm 2.5\,\mathrm{V}$. We were able to solve this problem by putting voltage dividers from the $5\,\mathrm{V}$ rails in front of the DIO port on the AD5235. The CLK speed was also slowed down such that the slew rate would not be a factor. By varying the resistances after the two potentiometers, we can use one channel as coarse tuning, and the other as fine tuning, thereby allowing more than 1024 steps of precision between the two extremes. After the voltages are summed, the resultant signal is sent through a current limiting resistor which is several orders of magnitude greater than the load resistance. This is merely a broad outline of the mechanics of the current source board. The schematic of the current source

can be seen in Figure A.1.

As mentioned in the SPI communications section (3.6.1), each new IC that the processor wishes to address increases the number of digital lines by one. However, biasing two MSAs would require four additional digital lines - one current bias and one flux bias per device. This becomes problematic for scaling as adding fiber optic lines increases the cost as well as the physical footprint of the current source. To address these limitations, a MCP23S08 was used as a multiplexer. With proper control of this IC, the user can leverage the chip's eight outputs as CS lines, effectively allowing eight CS lines to be controlled by a single CS line from the relay board. However, the introduction of this chip does introduce additional complication, as it requires a secondary CLK line for communication. Despite this additional fiber optic line, only four lines were necessary to communicate with eight chips; an improvement over the ten lines that would normally be necessary. In the iteration of the code used for this thesis, the EtherTen clock speed was set to 500 KHz, and with the AD5235 and MCP23S08 requiring 16 bits per command it can take an absolute minimum of 64 μs to send a command, without any added delays. This number could be brought lower by increasing the clock speed, however fast switching time was not a issue that we needed to address, so no work was put into optimizing the speed of altering the current.

Feedback from the current source can be achieved in two ways. First, a look up table can be made by placing dummy load on the output of the current source and recording the current through the load via conventional means. If the impedance of the dummy load matches that of a normal load, then the look up table can be used to determine the potentiometer values required to source the desired current. Second, the board comes patterned with a built-in readout system. The voltage drop over the current limiting resistor is measured by a differential op-amp and the value is sent back to the processor, which can then calculate the current. However, we did not get this aspect of the board fully operational, and it is left for future work.

Chapter 4

Low Temperature Characterization Work: Now That We Got Cold, What Did We Do?

4.1 Characterization of a Microstrip SQUID Amplifier

For both testing the cyrostat hold time, the custom electronics and data acquisition, and over ease of use for the system, several MSA were packaged and calibrated. This process was multifold, first an MSA chip was attached to an amplifier board, tested to ensure the functionality of the MSA, and then characterized if the MSA is a suitable first low noise amplifier. This process can take multiple cooldowns in several different cryogenic setups. The MSA that were used for testing were acquired from ez-SQUID [26].

4.1.1 MSA Board Design and Construction

An MSA when fabricated is roughly 1 mm x 1 mm chip and cannot be used without first being attached to larger structure. The chip itself contains the SQUID components: the

superconducting loop and input coil, as well as several large pads used for wire bonding. A picture of an MSA chip can be seen in Figure 2.9. This large structure is usually a printed circuit board (PCB), and is set up such that all inputs, wires, and auxiliary components can be physically secured. For this MSA, the auxiliary components consist of an external coil used for flux biasing, a current biasing line including RC filtering components, output filtering components, and an input and output SubMiniature version A (SMA). To incorporate all of these components, we use a design based on an MSA package by Michael Mück. The design can be seen in Figure 4.1a, and the equivalent circuit diagram in Figure 4.1b. The MSA chips are attached to the board with GE varnish, and the input and output pads are wire bonded from the chip to the PCB with gold wire. Two versions of the board were made so that an MSA chip could be assembled in the WNG or WG configuration (see section 2.2).

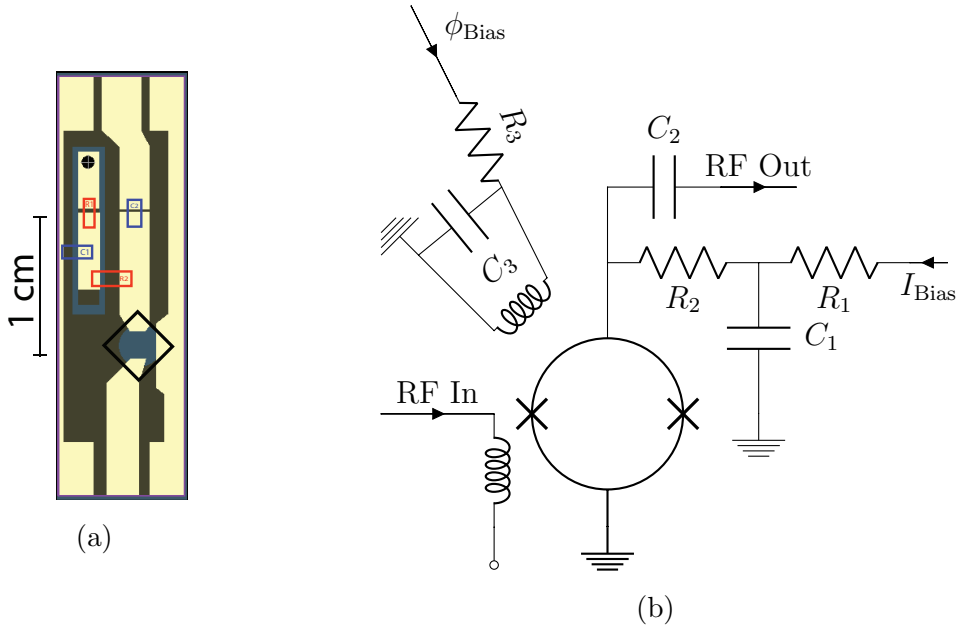

Figure 4.1: (a) Image of the MSA amplifer board in the WNG configuration. Small SQUID chip is attached over black box area. Capacitors locations are indicated in blue, and resistor locations are indicated in red. Location of coil is on opposite side of the board is not shown. (b) Electrical schematic of WNG board design.

The boards can be described as three separate section: the current biasing section, the flux biasing section, and the RF output section. The current biasing section includes components $R_1 = 100\Omega$, $R_2 = 621\Omega$, and $C_1 = 1\mu F$. A DC current is applied from a biasing source, which is sent through a low pass filter (R_1 and C_1), then through a large resistor (R_2, where $R_2 > R_1$) to further minimize any voltage noise. The flux biasing circuit is on the opposite side of the PCB (not shown in Figure 4.1a), where a current is applied to a small coil which is inductively coupled to the SQUID. The coupling coil is typically a 10 turn coil made from 38 American Wire Guage (AWG) copper wire, which is mounted to the PCB via GE varnish. A low pass filter ($R_3 = 1000\Omega$ and $C_3 = 1\mu F$) is also built into this section to minimize noise as well. The output of the SQUID is measured after the DC blocking capacitor (C_2). Components $C_2 = 1\mu F$ and R_2 must be chosen so that the impedance of R_2 is much greater than C_2 in the desired frequency range. This insures that large majority of the rf output signal passes through C_2 and is propagated through the rest of the system.

4.1.2 MSA Testing

Initial Testing

The MSAs were tested to determine if they were suitable for use as a first stage amplifier. First we had to determine if the chips had survived the fabrication and mounting procedure. A common way that an MSA can fail is when a voltage buildup causes a spark across the Josephson junction, effectively destroying the device. Furthermore, the mounting process has a chance to cause a spark across the junctions, but this risk can be minimized with proper care. In order to test if the device had survived, we attached an MSA chip to the previously described amplifier board, which was then attached to a characterized dip probe and submerged in LHe. The dip probe consisted of a long coaxial rf cable attached to several rf-attenuators. Pre-device attenuation was put in places so that the applied signal would not overload the MSA, and post-device attenuation was applied in attempt to dampening any resonances in the cable, which may cause unwanted feedback into the MSA. A diagram of the dip probe, along with the components, can be seen in Figure 4.2. To shield the MSA from electromagnetic noise, we surrounded it with a thin lead sheet

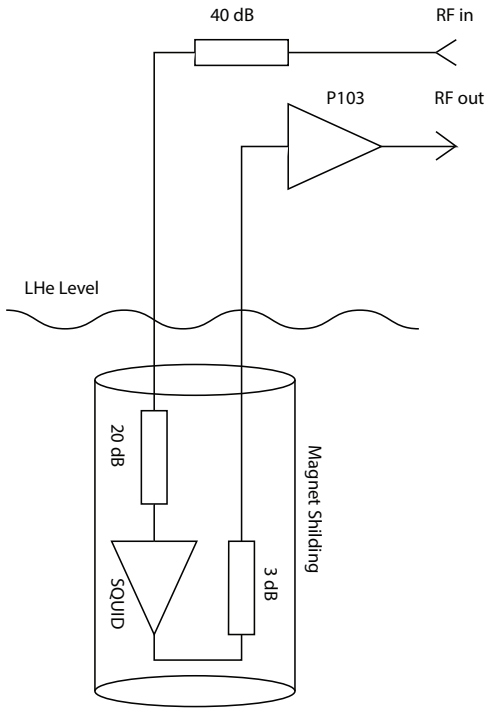

Figure 4.2: Illustration of the dip probe set up

which in turn was surrounded by Metglas. Lead is superconducting at LHe temperatures, therefore if it was cooled in a zero field environment, the Meissner effect should prevent the MSA being affected by any stray magnetic flux, and the Metglas provided further magnetic shielding.

An MSA was determined to be functional - however not necessarily suitable for experimental use - if the device could produce a noticeable gain. To test the gain, we applied a varying rf signal over the expected operational frequency range while altering I_{Bias}. The output of the MSA was monitored, with respect to the input signal, and when the gain achieved some maximum value ϕ_{Bias} was altered to achieve maximum gain. After this process was completed, the values of I_{Bias}, ϕ_{Bias}, and maximized normalized gain were noted for future use. However, just because a MSA passed this test does not mean that they were sufficiently characterized nor that they were suitable for experimental usage at low temperatures; further testing is necessary. This is because these tests were conducted at

LHe temperatures, and the MSA's characteristics could change in the sub-1 K range.

Sub-Kelvin Testing

Low temperature testing is necessary to determine the usability of the MSA. In this temperature range the device may have undesirable characteristics which may included hysteresis, high noise temperature, or low gain. While the device should have been fabricated in such a way to eliminate any hysteresis, it is possible for some of the aluminum to not have been properly oxidized, therefore when cooled below the T_c of aluminum, 1 K, the Stewart-McCumber parameter may change in such a way that the device becomes hysteretic. The noise temperature of the device should scale linearly with the physical temperature, however it is possible for a device to not follow this relationship.

To test an MSA in a sub-Kelvin environment, we installed the devices in our ADR cryostat. They were installed on the lowest temperature stage in a shielded enclosure, which included a lead-plated copper tube as the inner layer and cryoperm - a nickel-iron alloy with a very high magnetic permeability - enclosure as the outer layer for further magnetic shielding.

The devices were biased for maximum gain at 2.7 K, after which the system was adiabatically cooled to the system minimum temperature of 50 mK. Because some of the wiring used in the biasing lines consisted of normal metals, as well as superconducting metals, we expected both the applied current and flux bias to change slightly with temperature. Therefore, during the cooling process the output of the device was consistently monitored. Throughout the process, if the gain decreased slightly then the biasing was changed to re-achieve maximum gain. If any sudden change in gain was observed, the cooldown was stopped and the device was warmed slightly and re-cooled to see if the results were reproducible. If the sudden drop in gain was reproducible, and the high gain could not be re-achieved, then the device was determined to be hysteretic. It was throughout this process that any hysteretic devices were removed from the usable list. For the remaining devices, that were non-hysteretic and demonstrated high gain, we proceeded to measure their noise temperature.

4.1.3 Noise Temperature Measurements

After determining that an MSA was non-hysteretic, we measured the device's noise temperature. If the noise temperature decreased linearly with respect to temperature, we could then conclude that the device would be suitable as a first stage amplifier. Two ways of measuring the noise temperature of an MSA were attempted.

We first attempted to measure T_e by using the terminated resistor method as described in section 2.7.2. A 50Ω SMA terminator used to terminate the input of the MSA. To thermally isolate the MSA from the terminator, the terminator and MSA were placed on their own stages, both of which were weakly thermally linked to the FAA stage of the ADR, and were connected together by two long pieces of NbTi coax. Heaters and thermometers were placed on each stage so that we could monitor and control the temperatures independently. A diagram of our setup can be seen in Figure 4.3. Despite our attempts at thermal isolation, we found that the heat load on the system was high enough such that we could not keep the MSA temperature stable while changing the temperature of the 50Ω terminator.

Next we used a calibrated noise source to measure T_e. This method was more successful. We used a Hewlett Packerd 346B as our calibrated noise source. The 346B outputs an ENR of 15.6 dB at 100 MHz, which corresponds to a noise temperature of roughly $10,000$ K. The input noise to the MSA can be calculated by

$$T_{\text{input}} = n_3[n_2(n_1 * T_1 + T_2) + T_3] + T_4 \tag{4.1}$$

where n_i is the attenuation (or gain) in the signal line, which was calculated by $n = 10^{\text{attenuation in dB}/10}$, and T_i is the physical temperature of the n^{th} attenuator. From the equation it can be seen that the value and temperature of the final attenuator in the equation, n_3 & T_4, are the dominant factors in determining the input noise temperature. In practice, this is the final attenuator before the MSA, which is typically thermally tied to the lowest temperature stage. The size of all attenuators must be chosen such that the input noise will vary significantly depending on the status of the noise source. For our tests we had 40 dB of attenuation at room temperature, 3 dB at 50 K, 10 dB at 2.7 K, and 30 dB at the lowest temperature stage. A diagram of the setup for this test can be seen

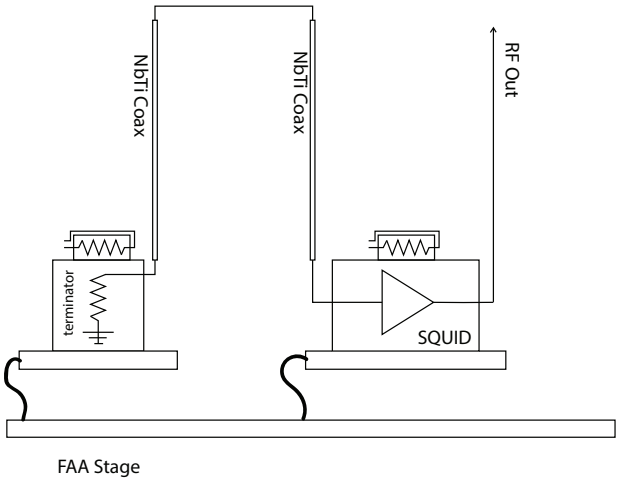

Figure 4.3: Diagram of setup to measure the noise temperature of a SQUID using the terminator resistor method. The thick lines indicates a weak thermal link between the two stages, and thin line between the two NbTi coaxes is a copper coax which is also thermally linked to the FAA stage.

in Figure 4.4. The results of these tests are shown in Table 4.1 and Figure 4.5. From the figure we can see that the T_e does follow T_{physical} with a near linear trend, as expected.

While the results of this noise measurement test do show the expected trend, the ENR was higher than the recommended value for making a noise temperature measurement within this range. Because of this issue, it is possible that the mismatch of impedance, coupled with the higher VSWR, may be grounds for being skeptical of the absolute answer of the previous measurement. We have included the work as a proof of principle - with the correct set up we can measure the noise temperature of an MSA with our cryostat. By using a lower ENR noise source, we could confirm the accuracy of the noise temperature measurement.

4.2 Automated Biasing Results

Independent from testing the MSAs as a first stage amplifier, they were also used to test the automated current source by proving that the current source could be used to properly bias

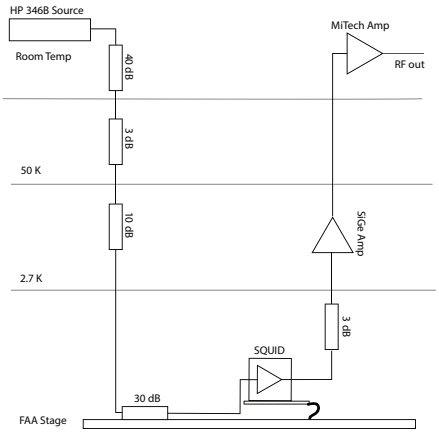

Figure 4.4: Diagram of testing setup used noise temperature test results shown in 4.1 and Figure 4.5. The dark line indicates a weak thermal link between the MSA stage and the FAA stage

MSA Temperature [K]	FAA Stage Temperature [K]	Power OFF [dBm]	Power ON [dBm]	Noise Temperature [K]
2.636	2.79	-86.402	-85.961	2.0391
2.163	1.938	-95.75	-95.13	1.4175
2.1595	1.9389	-95.909	-95.223	1.0678
1.579	1.8382	-98.68	-97.95	0.97109
0.7058	0.48978	-99.479	-97.422	0.34266
0.4345	0.22589	-100.51	-96.948	0.15869
0.3488	0.11293	-103.8	-99.233	0.14266

Table 4.1: Data collected from the calibrated noise source y-factor noise temperature measurement.

the devices. Several tests were conducted to illustrated the current source was working.

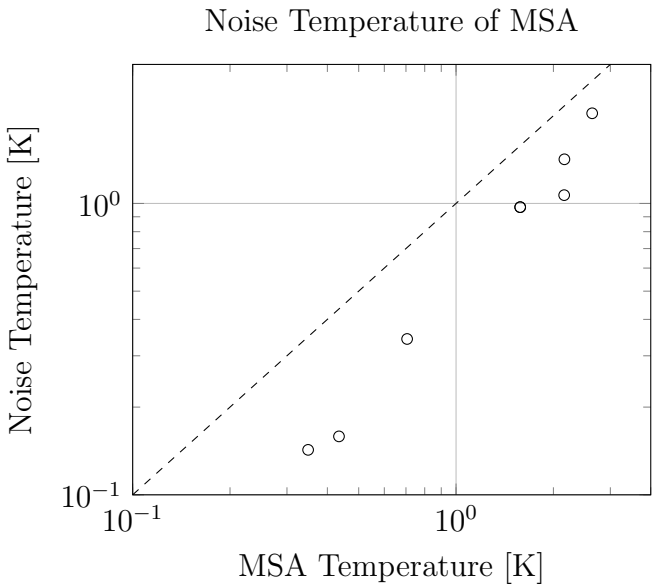

Figure 4.5: Post selected data of noise temperature of a Microstrip SQUID Amplifier using the calibrated noise source Y-Factor method. Dashed linear line added for reference.

Stability Test

First we tested the output stability of the boards. If the output voltage had large spikes, or dramatic shifts over time, then it would not be a suitable biasing source for an MSA. We performed both a longer term and a short term stability tests. For the long term test, the output was set to a constant voltage and we measured the voltage drop over a $10\,\Omega$ resistor with a E34401A digital multimeter, taking one measurement per second over 40 minutes. The result of the test are shown in Figure 4.6. A sudden shift was noticed in the output voltage over a ten minute interval causing the total variance in the output to be about 0.3%. This circuit uses five resistors per output channel, and surface mount resistors have a temperature dependence which can be up to 200 ppm/°C. The voltage supply and potentiometers have a temperature dependence of 15 ppm/°C and 35 ppm/°C [2, 1]. While this box was exposed to the room environment, and there could have been convection currents when the ICs were warm, this fast drift is larger than expected just from the resistors temperature dependence. Programmable feedback, as well as thermal

isolation, can be implemented for further stability.

For the short term test, the voltage was set to a specific value and the output was directly measured with the same multimeter as in the previous test. The results of the short term test are shown in Figure 4.7. The short term test was performed to check if there was a large drift or spike after setting the voltage. If the short term drift was dramatic, then compensation in setting the voltage in an experimental setting would need to be performed. However, we did not notice a drift that would warrant such an action, as the change was only around $8 \times 10^{-3}\%$.

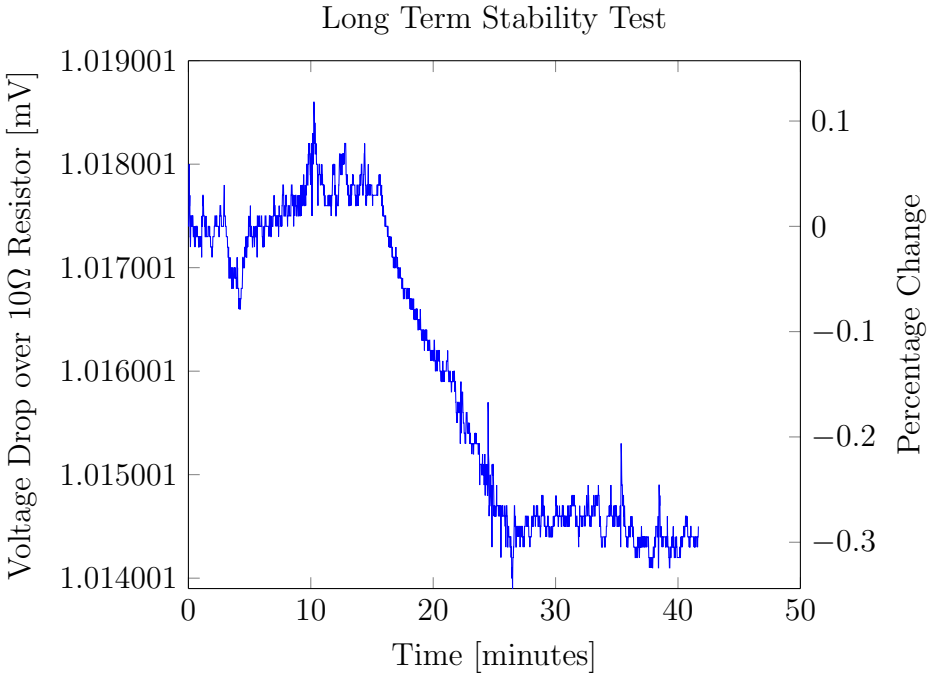

Figure 4.6: Long term stability test results. The automated biasing source was used to source a current and the voltage drop was measured over roughly one hour.

4.2.1 Biasing Results

After it was shown that the output voltage was relativity stable and could be programmed, the automated biasing board were tested on several MSAs. A calibrated dip probe testing

station was used for the following test. The automated current source was used to provide both I_{Bias} and ϕ_{Bias} to the MSA, and the board was powered via a wall-powered voltage supply.

First a 'mapping' test was performed. The mapping test consisted of applying a pure tone of 160 MHz, supplied by an Aglient E8254A signal generator, and measuring the gain and noise floor with a Hewlett Packard 8568B spectrum analyzer. While apply the tone I_{bais} and ϕ_{Bias} were swept. Then, by plotting the resulting signal to noise ratio ,we could determine where the MSA was properly biased and the program would record the biasing conditions. The data collected from one of these test can be seen in Figure 4.8, where the values on the x-axis represent the I_{Bias}, the values on the y-axis represent the ϕ_{Bias}, and the SNR is color coded where yellow indicates a higher SNR and blue a lower SNR value. The program can set the step sizes between I_{Bias} and ϕ_{Bias} independently.

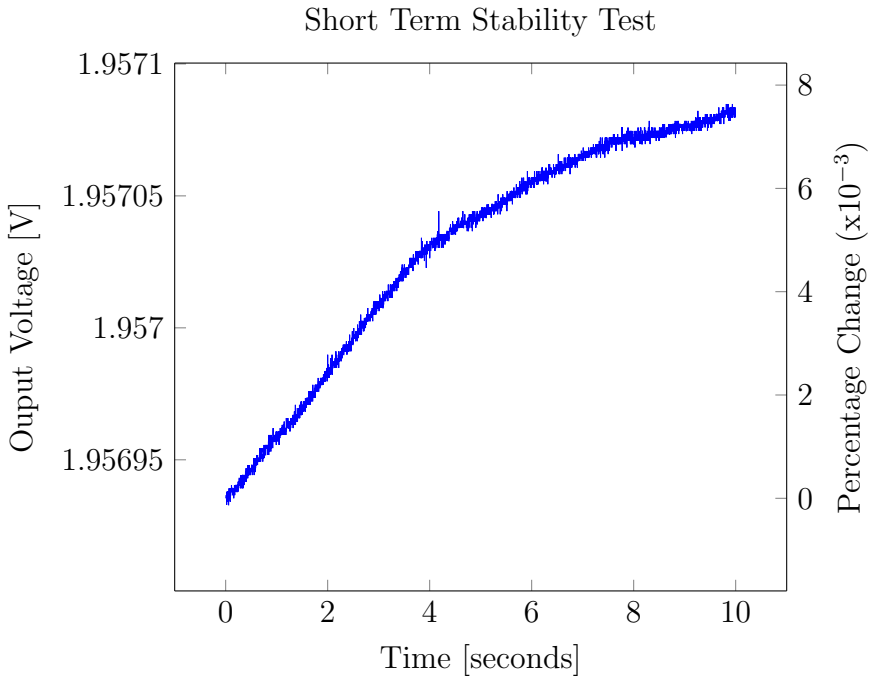

Figure 4.7: Short term stability test results. The direct output voltage was measured from the automated current source board.

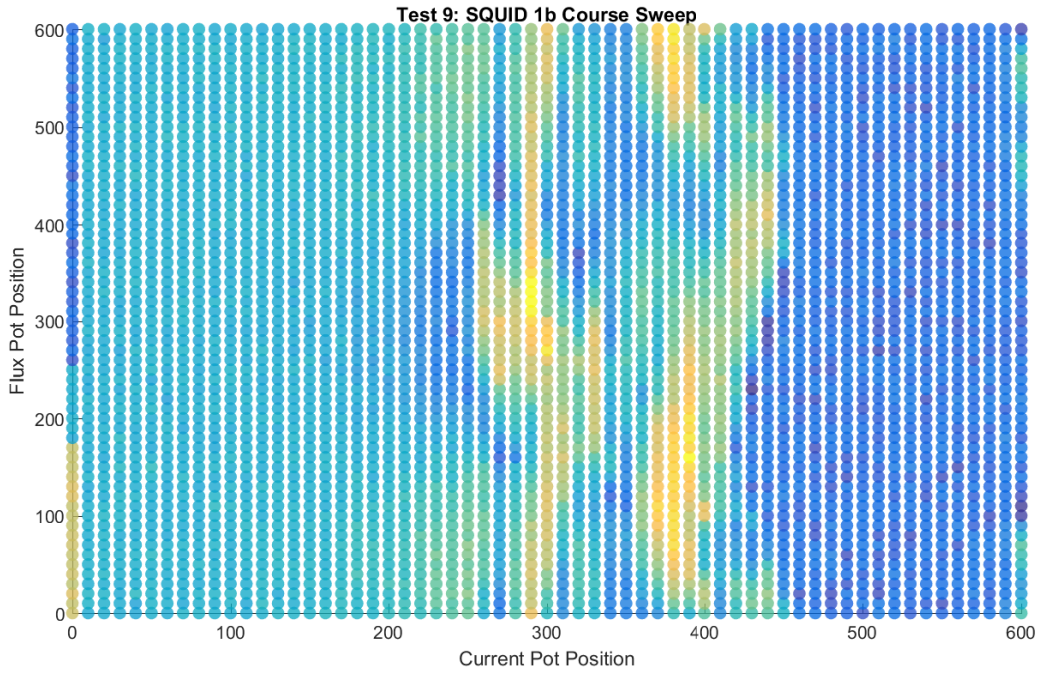

Figure 4.8: 'Heat map' of the signal to noise ratio of a MSA. Yellow indicates higher signal to noise ratio, and blue a lower signal to noise ratio The X-axis is a current bias of the MSA in arbitrary units, and the Y-axis is the flux bias in arbitrary units.

The second test consisted of current biasing the MSA and altering ϕ_{Bias}. From the results of the first set of tests, we know the values of I_{Bias} which would result in a proper current bias, and set I_{Bias} to those values. Using the same setup as in the previously described test, we swept though the range of ϕ_{Bias}, for both I_{Bias} values that produced the highest SNR value. The results of this test can be seen in Figure 4.9. The purpose of this test was to show that we were able to sweep through a full value of Φ_0, also to see if there was a noticeable difference in the gain between the two candidate values of I_{Bias}.

The final set of tests were much like the first test described, where we altered both I_{Bias} and ϕ_{Bias}, however instead of using a pure tone and measuring the signal and noise, an Aglient E5071C network analyzer was used to both sweep the applied frequency and measure the resulting signal. By using a network analyzer, over a spectrum analyzer, we

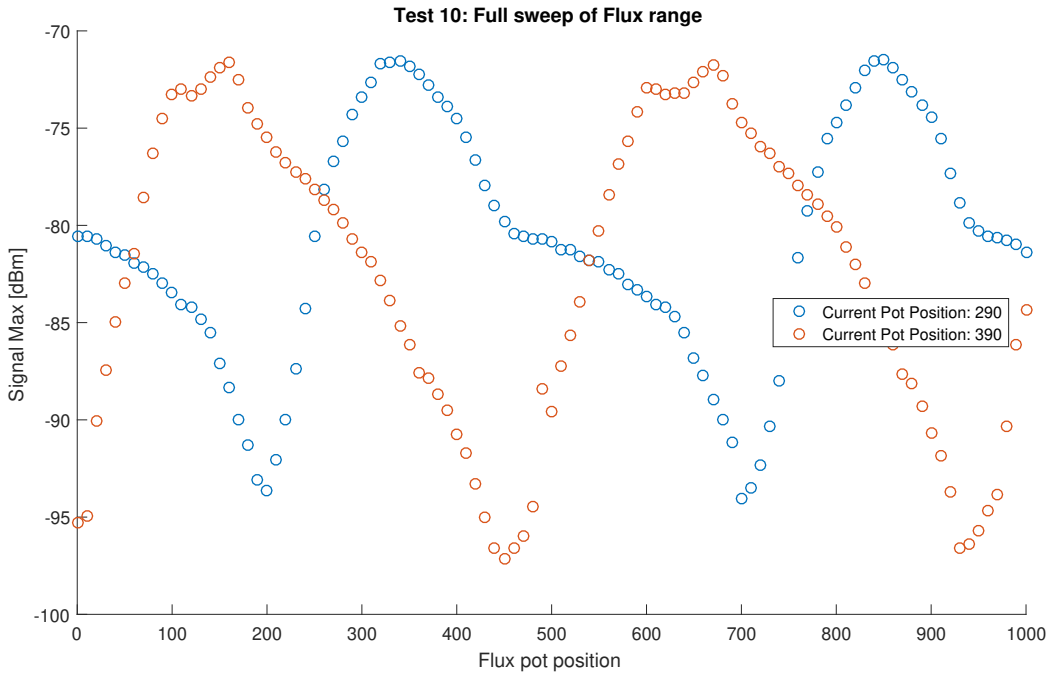

Figure 4.9: Gain of an MSA as the flux is biased from $-50\mu A$ to $+50\mu A$. It can be seen that the course can sweep a full flux phase. The X-axis the flux bias in arbitrary units, and the Y-axis is the signal strength of the system in dBm.

can easily compare the output power to the applied power. By first taking a calibration sweep of the system without the MSA, we can calibrate the gain of all the other components in the system. Thereby allowing us to isolate the gain due to the MSA.

The test procedure was to apply I_{Bias} and ϕ_{Bias}, then the network analyzer would sweep through the set frequency range. After the network analyzer saved the resulting data, the ϕ_{Bias} value would increment. After ϕ_{Bias} finished stepping through the programmed range, I_{Bias} would be incremented and ϕ_{Bias} would be reset to its starting value. This process would continue until for all programmed values of I_{Bias}. With this program we get one image per I_{Bias} value, where Figure 4.10a is an example of one of these image. This image can be freely rotated in MATLAB, the program in which the data was collected and plotted, allowing the user to highlight the data they deem most valuable. Using the collected data,

a ‘heat map’ much like Figure 4.8 can be made. The corresponding heat map image can be seen in Figure 4.10b.

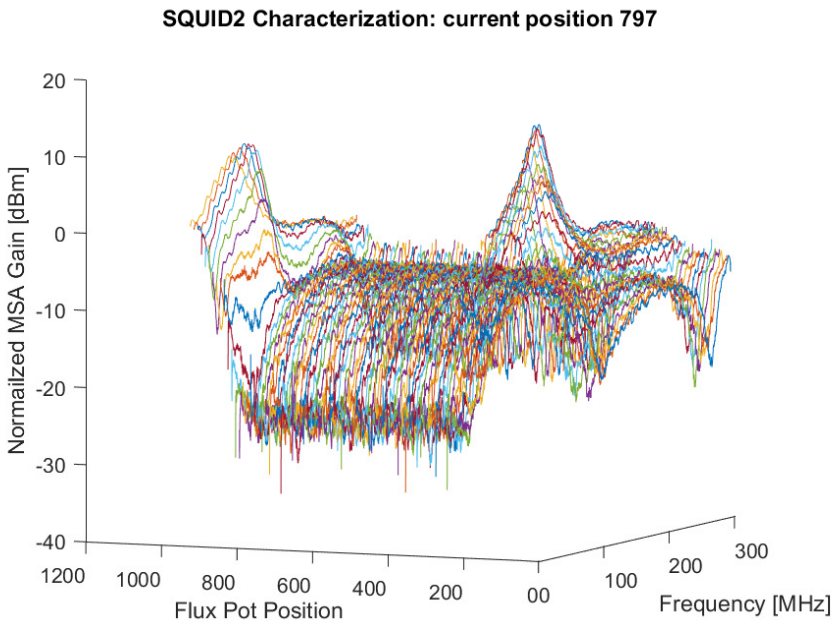

(a)

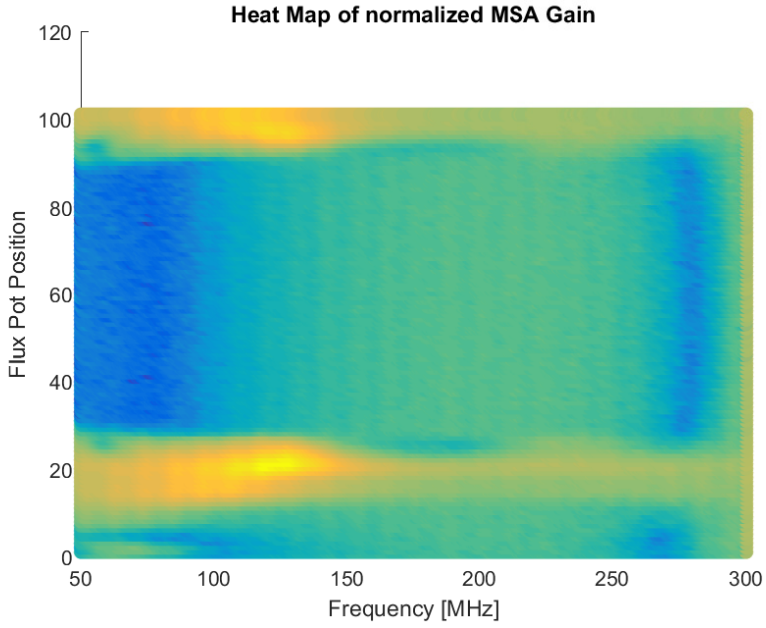

(b)

Figure 4.10: (a) Image from sweeping the applied frequency and ϕ_{Bias} for a single value of I_{Bias} (b) 'heat map' of 4.10a, where yellow indicates a higher recorded gain, and blue indicates a lower recorded gain value.

4.3 MSA Input Coil Cutting

As was shown section 2.2.1, the length of the input coil is directly correlated with the operational frequency of an MSA. Furthermore, in an earlier paper on MSA[27], it was shown that the portions of a coil can be removed from a patterned MSA via ion etching. As expected, this process increased the operational frequency without altering the gain. A more convenient method was attempted, where a laser cutter and microscope were used to ablate the open end of the input coil, while the device was attached to the RF board.

The principle behind this experiment was to use a laser cutter to remove sections of the open end of the input coil. The removal of the coil can be achieved by either ablating the floating end of the coil, or causing an electrical break between two portions of the coil. By ablating the coil, or causing an electrical open circuit within the coil, the effective coil length can be shortened, causing the operational frequency of the MSA to increase. From previous works it has been shown that the operational frequency of the MSA and the coil length are inversely proportional, however there is not an exact equation that can be used to fit the coil length to the resonant frequency [27, 8]. This ablation technique allows low frequency MSAs to be individually tuned for potentially any desired experiment, eliminating some of the problems that come from not being able to precisely determine the operational frequency of the MSA from patterning conditions. This technique could be useful for tuning large arrays of MSAs in which all the resonators need to be set to a specific frequency range.

4.3.1 Laser Cutting

A New Wave Research LCS-II 532 laser cutter, mounted on an optical microscope, was used to ablate the input coil. The LSC-II outputs a 532 nm beam with an output power that can be varied up to 2 mJ. The beam was then focused through a Mitatoyo M Plan APO 100x and, using the built in x-y shutters, was aligned to remove only the desired area. For this test we used an unmodified 60 turn MSA purchased from ez-SQUID [26]. The MSA was secured to a PCB by GE varnish, and the inputs of the MSA were wire bonded to the PCB, as described in 4.1.1.

To initially test that the laser could ablate the coil, the DC resistance of the input coil was measured with a multimeter while successive pulses were applied to a small section of a single coil. After six pulses, at the power of roughly 1.3 mJ [30], the coil was sufficiently removed to measure a break in the connectivity. This cutting parameter, six pulses at a power of 1.3 mJ, will be referred to as "cutting parameter one" for the rest of the section. Initially, the results of the cutting process were only observed via optical microscopy.

Cutting Parameter One Results

The first batch of tests consisted of removing several of the outermost turns of a 60 turn input coil. Cutting started from the open end of the coil; two coil turns were removed at a time with a single pulse. Removing multiple turns per test was done to both increase the shift in frequency per test, as well as to save time. Testing of the devices was done by dunking the MSA in a liquid helium dewar, with all cables and post MSA amplifiers normalized. Results of the test are presented in Figure 4.11.

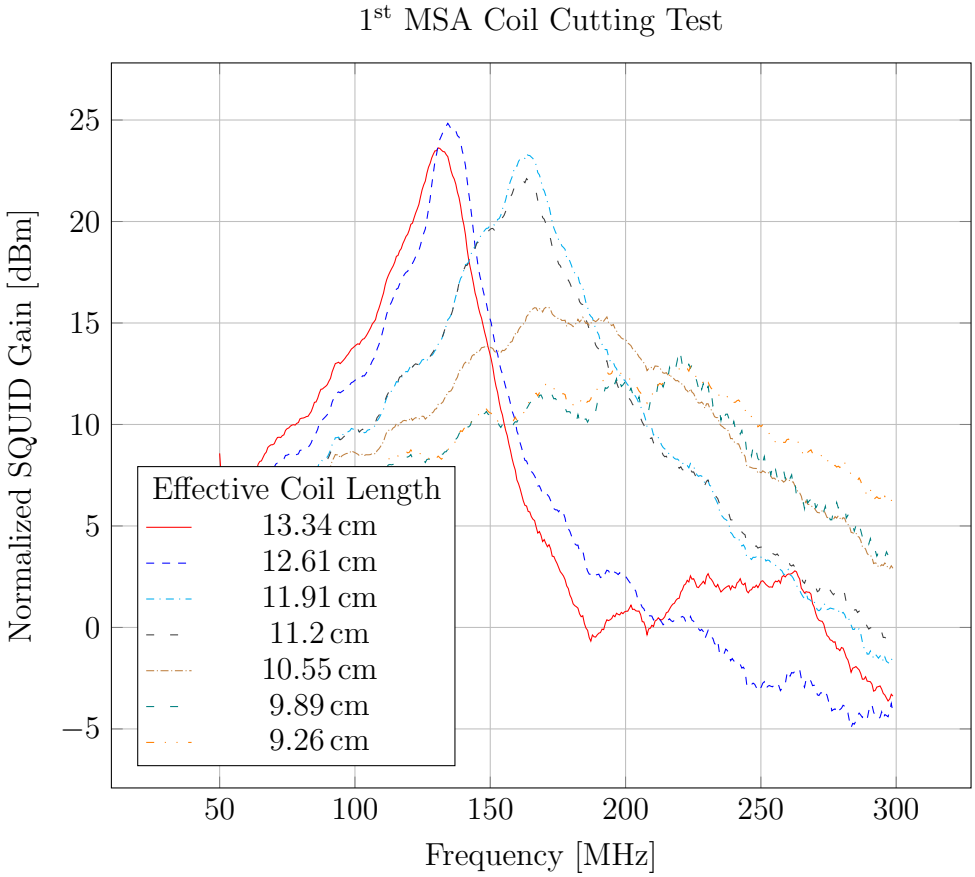

Figure 4.11: Change of resonant frequency of the first MSA after ablating complete coil lengths, with the cutting parameters of 1.3 mJ for more than 6 pulses.

It can be seen that the shift in the operational frequency from this test is very non-uniform and that the gain suddenly drops from 23 dB to 15 dB. We assume that this was because at some point during the fourth cutting procedure, the laser ablated through the SiO_2 layer. Later, we were able to show that applying more that 8 pulses at 1.3 mJ can ablate all of the insulating SiO_2. The theory is that one or more cuts damaged part of the square washer. While we are unsure of what the damage could have been, we hypothesize that the excessive ablation could have caused: a hole in the washer, some portion of the washer to no longer be a superconductor, or even some other problem. Furthermore it can

be seen that ablating the coil did not cause a very noticeable shift in frequency, as the effective coil lengths of 12.42 cm and 12.09 cm as well as the lengths of 11.4 cm and 10.7 cm look very similar. Unfortunately, I do not have a complete theory on why the ablation process for this MSA yielded these results, besides noting that the first ablation procedure was bad.

4.3.2 Atomic Force Microscopy of the MSA

After we had seen the drop in gain from the first cutting procedure, an atomic force microscopy (AFM) setup was used (from the University of Waterloo Watlabs) to determine the amount of material removed for various levels of power and number of pulses. From initialization test of scanning over a junction, we was found that the thickness of the input coil and SiO_2 layers was about 50 nm and 200 nm thick, respectively. Ideally, we would want our ablating procedure to remove the 50 nm of coil and only slight ablate into the SiO_2. To test the affects of both the number of pulses and the power applied per pulse, a grid of ablation tests was preformed on a spare input washer, where both the power and number of pulses were altered. We applied ablation power ranging from 0.68 mJ to full range of 2 mJ and varied the number of pulses from one to twelve. As previously alluded to, we were able to measure cutting parameter 1 and saw that applying 1.3 mJ at ten pulses and above was shown to ablate through the 200 nm of SiO_2 and into the Nb washer. During the first set of test, this number of pulses was applied multiple times. The increased number of pulses was done because I was unaware that ablating past the SiO_2 could be a possibility, and by only relying on optical observations to determine if the coil was ablated lead me to apply more pules than necessary. Also from these tests we found that a single pulse at about 1.8 mJ, was sufficient to ablate the entire thickness of coil and about 10 nm of the SiO_2 beneath the coil. The resulting AFM image and data can be seen in Figure 4.13. We called single pulse at 1.8 mJ "cutting parameter two". The optical difference of the cutting parameters can be seen in Figure 4.14.

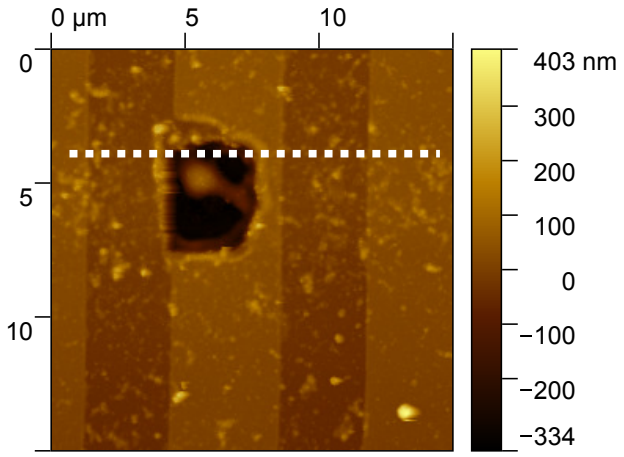

(a)

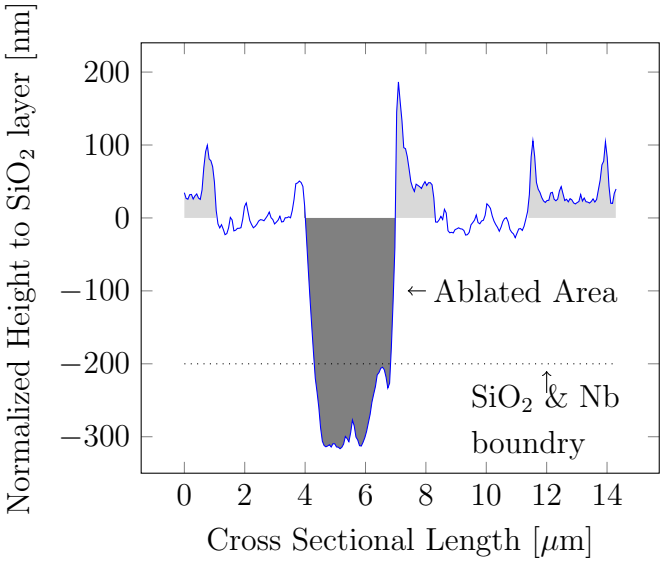

(b)

Figure 4.12: AFM Scan of the input coil after 10 pulses at 1.3 mJ. (a) AFM image of the ablated area.(b) Cross-sectional scan of white line in AFM image. Area shaded in dark grey is the section of the Nb input coil and SiO_2 substrate ablated by the laser pulses. As can be seen, the ablation removed the substrate and started to damage the Nb washer.

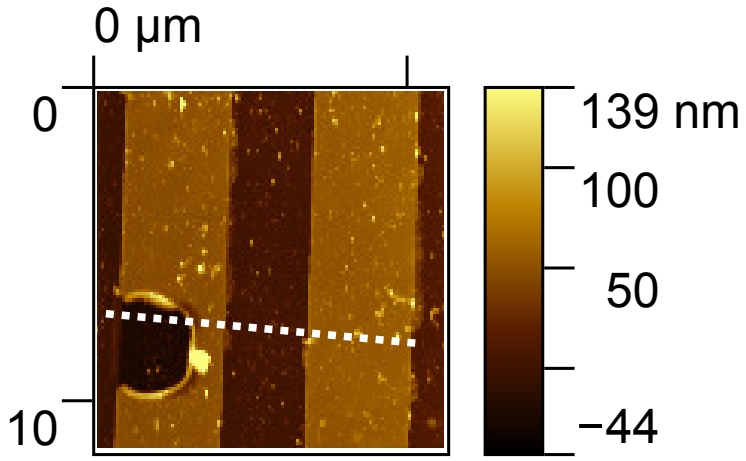

(a)

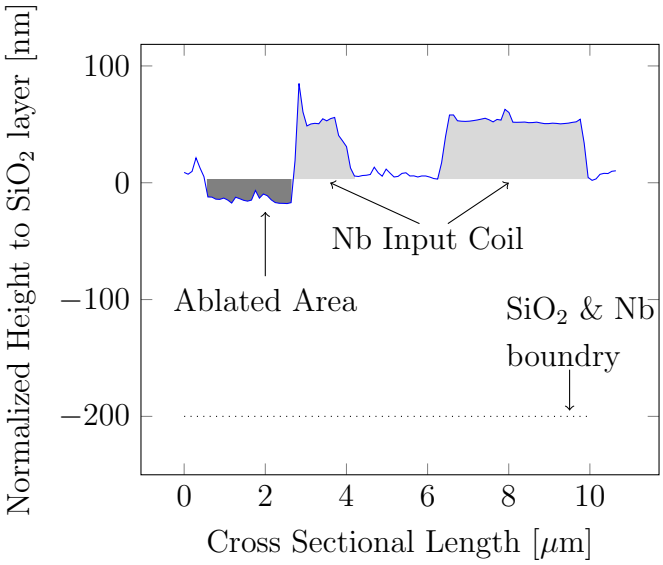

(b)

Figure 4.13: (a) AFM scan of the input coil after single pulse at roughly 1.8 mJ. The white line indicates the 2-D data slice shown in (b). (b) The light gray area is a cross section of a unaltered section of coil; the dark gray area is the result of a 1.8 mJ pulse on a section of coil. The dotted line indicates the depth of the SiO_2 layer.

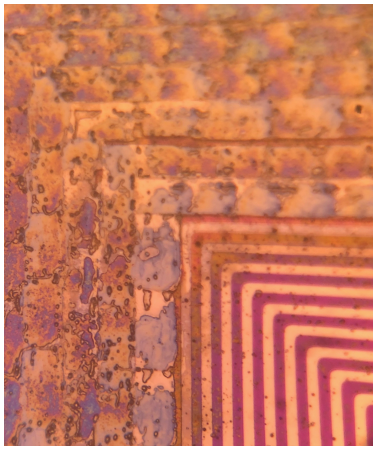

(a) Cutting Parameter One

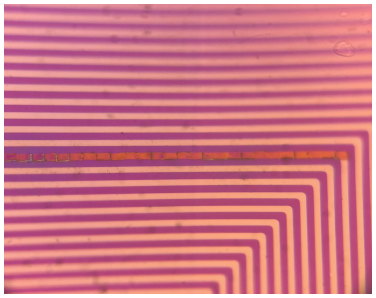

(b) Cutting Parameter Two

Figure 4.14: Comparison of the two different cutting parameters. (a) is the first cutting parameter of 6-10 pulses at 1.3 mJ. (b) is the second cutting parameter of a single pulse at 1.8 mJ. In the second only a single coil was ablated at a time, instead of two at a time as in the first; this was because we wanted to test if removing a single coil would be still cause a shift, however this still may be optimal because of the potential damage to the square washer if the higher power laser was focused directly onto the SiO_2 layer.

Cutting Parameter Two Results

A second MSA, was ablated with the second cutting parameters. Furthermore, in order to avoid potential damage to the square washer, only a single coil loop was ablated at a time. Another modification to the testing procedure was that, instead of removing the entire turn as was done in the first test, only a single side of the square loop was removed (refer to Figure 2.11b to see square turn input coil).

An initial measurement was made before current, as well as two measurements after the 20th turn and 40th turn had a single side removed, as seen in Figure 4.15. As before, the ablation of the coil should leave the maximum gain of the MSA unaffected; in these tests any loss of gain can be attributed to small changes in biasing parameters. During these tests a clear shift of resonant frequency can be observed. The frequency of maximum gain was shifted from an initial value of 190 MHz to 235 MHz when a single side of the

20^{th} turn of the coil was removed, and then to 258 MHz when a single side of the 40^{th} turn of the coil was removed. However, the shift in frequency is not as great as that reported in Mück's original paper [27]. Whereas their paper showed an increase of the resonant frequency from roughly 200 MHz to 630 MHz, as the coil length was changed from 77 mm to 7 mm, showing roughly a factor of three increase in resonant frequency, our results only showed an increase in resonant frequency by about a factor of 1.3. While this could be because we were not removing the full length of the coil, thereby allowing the attached section of the input coil to interact with the nominally non-active section of the coil by still being weakly capacitively coupled, we do not believe this to be the case because we would expect this coupling to broaden the resonance, which we did not observe. From the second batch of tests we were able to conclude that ablating the coil is a quick and useful technique in altering the operational frequency of an MSA and does not degrade the SQUID performance.

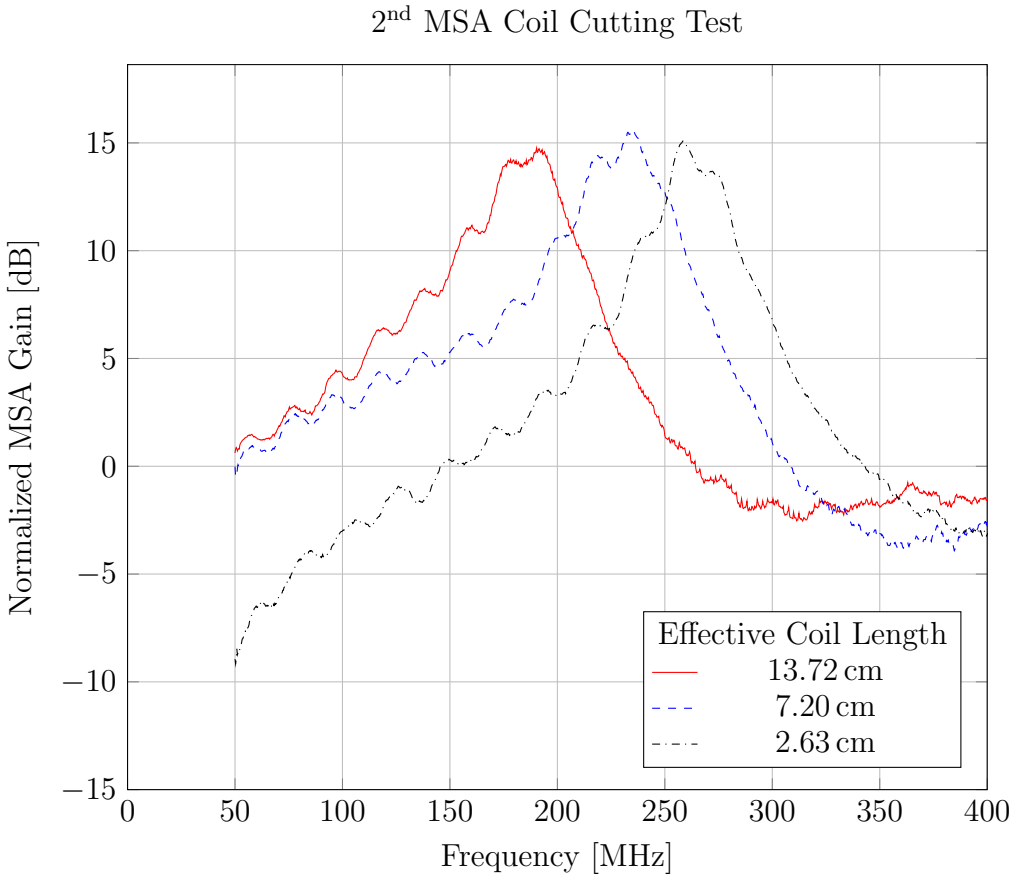

Figure 4.15: Change of resonant frequency of a MSA when ablating a single side of the 20^{th} and 40^{th} coil turn. Legend indicates the total coil length along with effective coil length after ablation process.

Chapter 5

Conclusion

In conclusion I was able to complete many of the goals set out during this thesis project. I was able to construct an ADR cryostat system and add the supporting electronics such that multiple types of components could be tested. We added a new support structure to the ADR, with carbon fiber archery arrows as a new, novel, and cheap building material. The thermal conductivity, and physical strength of these carbon fiber shafts were measured, and the results were published in reference [33]. We determined that we could machine away parts of the material could be machined away, which did decreased the thermal conductivity as desired, however in doing so the structural strength, the bending stiffness and spring constant, fell much faster than the decrease of thermal conductivity. Yet, it is our impression that the carbon fiber shaft, unmachined, a better strength to thermal conductivity ratio other cryogenic insulators. With the current design we estimate that the support structure could easily hold 10 kg, however we can not guarantee that the ADR would be able to cool down this mass to the desired temperature. Multiple computer programs were written to control several existing electronics. These programs allowed measurements to be made quickly. An rf switching system was introduced that will allow us to test multiple cryogenic components in a single cooldown. A custom computer controlled SQUID biasing board, able to bias multiple SQUIDs, was designed and implemented.

Multiple MSAs were constructed and tested. We were able to measure the noise temperature of these MSA and found devices that were able to function as an excellent first

stage amplifier with a noise temperature of 348 mK at 160 MHz. The measured noise temperature of the SQUID decreased proportionally with physical temperature, as expected. We were able to show that the automated biasing boards could provide the correct I_{Bias} and ϕ_{Bias} to an MSA, and the automated sweeping program allowed for broad characterization of the MSA.

Independently of measuring SQUIDS as a first stage amplifier, we were able to show that we are able to modify the input coil of an MSA to increase the operational frequency range. This was a new technique that consisted of using a laser cutter to ablate the input coil. Where it was previously shown that modification of the input coil would shift the operational frequency, this new technique is much quicker, only taking about 10 minutes to perform the cuts as described in section 4.3.2. Furthermore, this process does not require the SQUID to be dismantled from an amplifier board, nor does it need lithography techniques such as spinning resists, exposure with a mask aligner, and the ion etching.

Future Work

Improvements can still be made to the system and the supporting electronics. The heat load on the cryostat can be further reduced by altering the leg design to remove more material. The aluminum in the structural support system can be replaced by copper to further reduce the heat load on the system, and the design of the leg structure can be altered to minimized the use of vertical legs. Both of these changes should increase the hold time of the system.

Adjustments for noise temperature measurement can be made to further increase our sensitivity. These adjustments can be further optimization of the readout, and use of the calibrated noise source.

The automated current source can be further optimized. By insulating the box the stability of the system can be further increased. More research can be put into determining the cause of the shift in output voltage, and address the problem. The read-back system still needs to be implemented and optimized, and once the system is fully operational a program which can automatically keep an MSA biased, even through temperature drifts, can be designed.

However, even without any of the previously mentioned improvements, that cryostat is in working operation to test a wide variety of low temperature components, as desired.

References

[1] Analog Devices. *Nonvolatile Memory, Dual 1024-Position Digital Potentiometer*, 2012. Rev. F.

[2] Analog Devices. *Pin Programmable, Percision Voltage Reference*, 2012. Rev. C.

[3] S. J. Asztalos, G. Carosi, C. Hagmann, D. Kinion, K. Van Bibber, M. Hotz, L. J Rosenberg, G. Rybka, A. Wagner, J. Hoskins, C. Martin, N. S. Sullivan, D. B. Tanner, R. Bradley, and John Clarke. Design and performance of the ADMX SQUID-based microwave receiver. *Nuclear Instruments and Methods in Physics Research, Section A: Accelerators, Spectrometers, Detectors and Associated Equipment*, 656(1):39–44, 2011.

[4] S. J. Asztalos, G. Carosi, C. Hagmann, D. Kinion, K. Van Bibber, M. Hotz, L. J. Rosenberg, G. Rybka, J. Hoskins, J. Hwang, P. Sikivie, D. B. Tanner, R. Bradley, and J. Clarke. SQUID-based microwave cavity search for dark-matter axions. *Physical Review Letters*, 104(4):1–4, 2010.

[5] M Barucci, S Di Renzone, E Olivieri, L Risegari, and G Ventura. Very-low temperature specific heat of Torlon. *Cryogenics*, 46(11):767–770, 2006.

[6] C. A. Bryant and P. H. Keesom. Low-Temperature Specific Heat of Indium and Tin. *Physical Review*, 123(2):491–499, 1961.

[7] John Clarke and Alex I. Braginski. *The SQUID Handbook*, volume 1. Wiley-VCH Verlag GmbH & Co. KGaA, Weinheim, FRG, may 2005.

[8] John Clarke and Alex I. Braginski. *The SQUID Handbook Vol. II*, volume 2. Wiley-VCH Verlag GmbH & Co. KGaA, Weinheim, Germany, aug 2006.

[9] David Cohen, Edgar A Edelsack, and James E Zimmerman. MAGNETOCARDIOGRAMS TAKEN INSIDE A SHIELDED ROOM WITH A SUPERCONDUCTING POINT-CONTACT. *Applied Physics Letters*, 16(7):278–280, 1970.

[10] Robert J. Corruccini and John J Gniewek. *Specific Heats and Enthalpies of Technical Solids at Low Temperatures: A Compliation from Literature*. United States Government Printing Office, 1963.

[11] W.J De Haas, E.C Wiersma, and H.A Kramers. Experiments on adiabatic cooling of paramagnetic salts in magnetic fields. *Physica*, 1(1):1–13, 1934.

[12] P. Debye. Einige Bemerkungen zur Magnetisierung bei tiefer Temperatur. *Annalen der Physik*, 386(25):1154–1160, 1926.

[13] Kisaburo Deguchi, Takehiko Ishiguro, and Yoshiteru Maeno. Field-orientation dependent heat capacity measurements at low temperatures with a vector magnet system. *Review of Scientific Instruments*, 75:1188–1193, 2004.

[14] Inc. High Precision Devices. Cryostat model 106 shasta — hpd, 2019.

[15] W. F. Giauque. A thermodynamic treatment of certain magnetic effects. A proposed method of producing temperatures considerably below 1° absolute. *Journal of the American Chemical Society*, 49(8):1864–1870, 1927.

[16] W. F. Giauque and D. P. MacDougall. Attainment of temperatures below 1$\hat{c}irc$ absolute by demagnetization of $gd_2(so_4)_3 \cdot 8h_2o$. *Physical Review*, 43(9):768–768, 1933.

[17] W. E. Gifford and R. C. Longsworth. Pulse-Tube Refrigeration. *Journal of Engineering for Industry*, 86(3):264, 1964.

[18] Mike Grusin. Serial peripheral interface (spi). https://learn.sparkfun.com/tutorials/serial-peripheral-interface-spi/.

[19] Cryomech Inc. Pt410 cryocoolers, 2019. https://www.cryomech.com/products/pt410/.

[20] Cryomech Inc. Pulse tube cryocoolers, 2019. https://www.cryomech.com/cryocoolers/pulse-tube-cryocoolers/.

[21] High Percision Devices Inc. *Installation and Operation Manual*. HPD.

[22] B.D. Josephson. Possible new effects in superconductive tunnelling. *Physics Letters*, 1(7):251–253, 1962.

[23] Keysigh Technologies. Noise Figure Measurement Accuracy : The Y-Factor Method. Technical report, Keysight Technologies.

[24] M. W. Meisel, G. R. Stewart, and E. D. Adams. Thick film chip resistors as millikelvin thermometers. *Cryogenics*, 29(12):1168–1169, 1989.

[25] E. I. Mikulin, A. A. Tarasov, and M. P. Shkrebyonock. Low-Temperature Expansion Pulse Tubes. In *Advances in Cryogenic Engineering*, pages 629–637. Springer US, Boston, MA, vol 29 edition, 1984.

[26] Michael Mück. ez SQUID. "http://www.ez-squid.de".

[27] Michael Mück, Marc Olivier André, John Clarke, Jost Gail, and Christoph Heiden. Radio-frequency amplifier based on a niobium dc superconducting quantum interference device with microstrip input coupling. *Applied Physics Letters*, 72(22):2885–2887, 1998.

[28] Michael Mück, Marc Olivier André, John Clarke, Jost Gail, and Christoph Heiden. Microstrip superconducting quantum interference device radio-frequency amplifier: Tuning and cascading. *Applied Physics Letters*, 75(22):3545–3547, 1999.

[29] Michael Mück, Bernd Schmidt, and John Clarke. Microstrip superconducting quantum interference device amplifier: Operation in higher-order modes. *Applied Physics Letters*, 111(4), 2017.

[30] New Wave Research. *Operator's Manual QuikLaze, QuikLaze II & QuikLaze FE*. Number July. 2000.

[31] C. I. Nicholls and H. M. Rosenberg. The thermal conductivity of carbon - carbon fibre composites below 80 K. *Cryogenics*, 24(7):355–358, 1984.

[32] E.R. Parker. *MATERIALS DATA BOOK. For Engineers and Scientists.* 1 1967.

[33] C. E. Plesha, E. M. Tonita, and J. B. Kycia. Note: Carbon fiber composite arrow shaft as cryogenic structural support material. *Review of Scientific Instruments*, 89(12):126105, 2018.

[34] Frank Pobell. *Matter and Methods at Low Temperatures.* Springer, 3rd edition, 2007.

[35] J A Quilliam, S Meng, H A Craig, L R Corruccini, G Balakrishnan, O A Petrenko, A Gomez, S W Kycia, M J P Gingras, and J B Kycia. Juxtaposition of spin freezing and long range order in a series of geometrically frustrated antiferromagnetic gadolinium garnets. *Physical Review B*, 87(17):174421, 2013.

[36] M. C. Runyan and W. C. Jones. Thermal conductivity of thermally-isolating polymeric and composite structural support materials between 0.3 and 4 K. *Cryogenics*, 48(9-10):448–454, 2008.

[37] Shaowei Zhu, Peiyi Wu, and Zhongqi Chen. Double inlet pulse tube refrigerators: an important improvement. *Cryogenics*, 30(6):514–520, 1990.

APPENDICES

Appendix A

Schematics for Automated Current Source

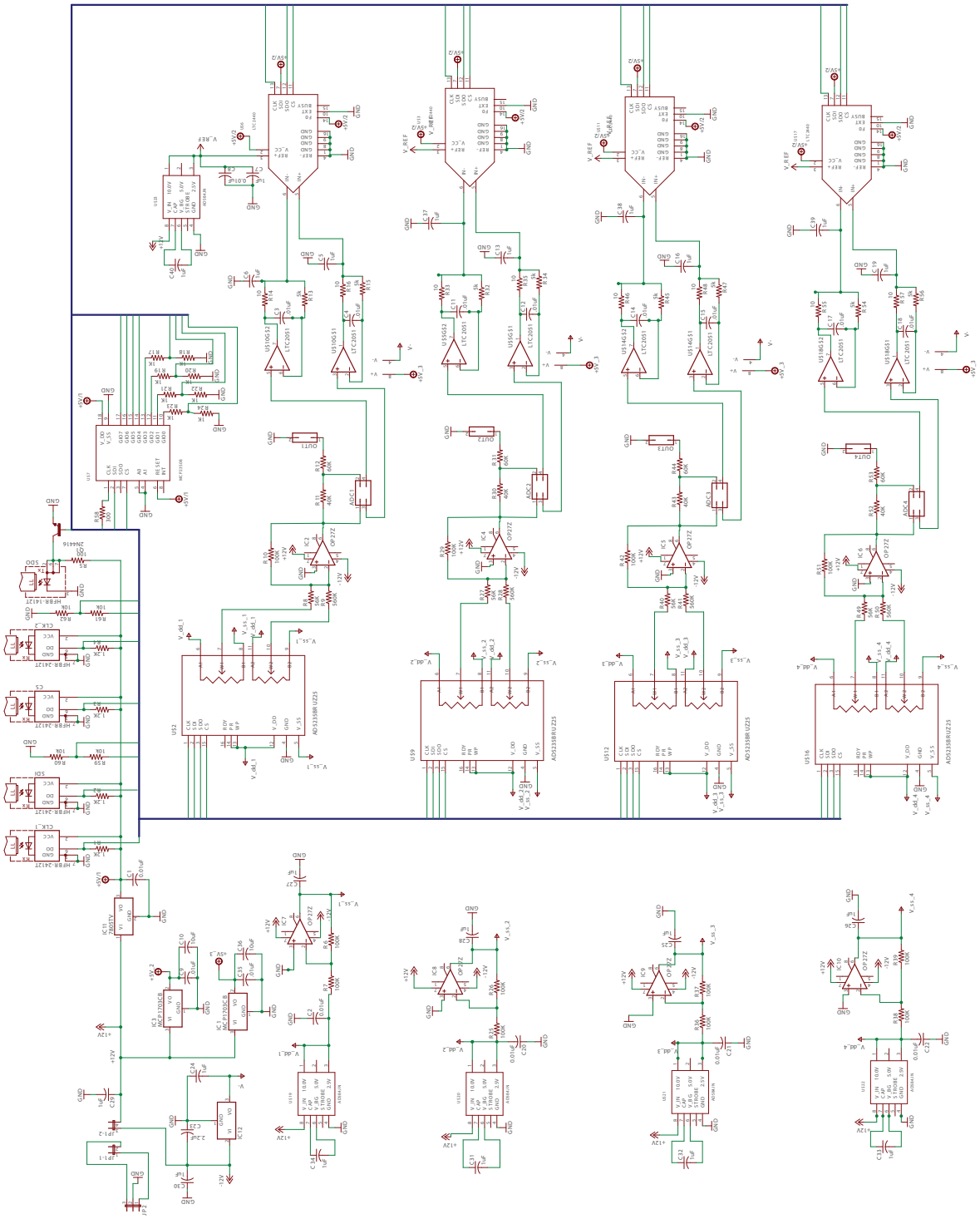

Figure A.1: Schematic for Current Source

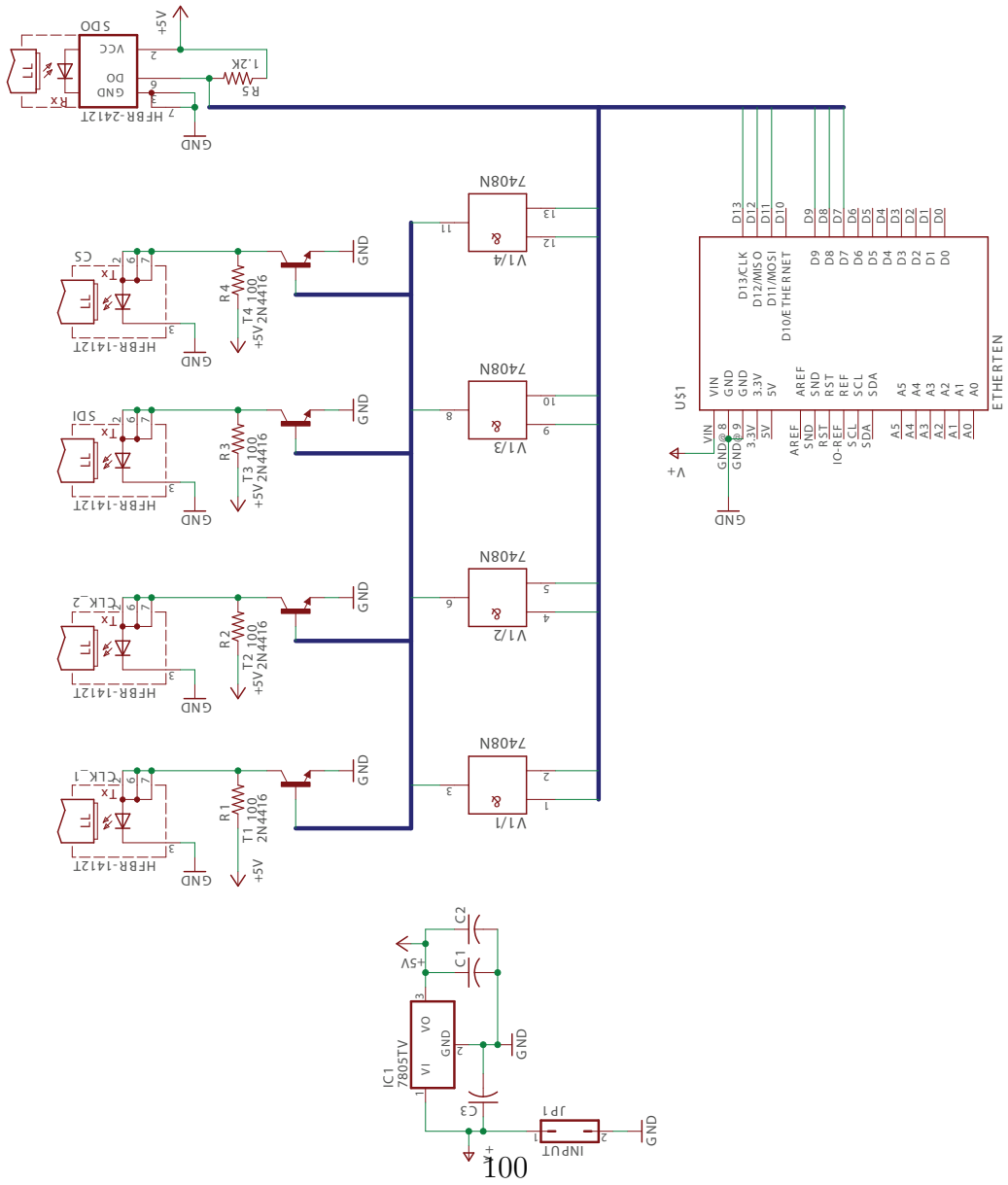

Figure A.2: Schematic for Current Relay

Appendix B

Code Repositories

The Arduino Code specifically mentioned throughout this thesis can be found in a gitHub repository: "https://github.com/cliffplesha/AutoamtedCurrentSource". The goal of posting the code it to give others who wish to reproduce this work, or use the current source for their own projects, a starting ground. I make no promise that the code is optimized, fully functional, or without errors.

The Arduino code was compiled on Arduino's published IDE at https://www.arduino.cc/en/Main/Software

Appendix C

Cooling Down the ADR Experiment - Advice on Running the Experiment

During the work described in this thesis, a ramp rate of $0.06\,V$ was initially used, however the ramp rate can be increased, or decreased, throughout the ramping procedure, as the magnet warms up due to the heat of magnetization. The superconducting leads have a critical temperature of 7 K in zero field, so do not let the temperature get above this value. If the temperature continues to rise, stop the ramping procedure, and if that does not work verify that the heat switch is off.

At the rate of 0.06 V it nominally takes an 1.5 hours to ramp from zero to full field, of 10 amps, which corresponds to a field of 4 Tesla at the salt pills.

The de-ramp rate is usually set to 0.05 V until the temperature reaches 1.2 K, at which point the rate is decreased to about 0.03 V. We expect to get to the 200 mK range with about $\frac{1}{3}^{\text{rd}}$ of an amp left in the magnet.